

On-chip Spin-Photon Entanglement based on Photon-scattering of a Quantum Dot

Ming Lai Chan,^{1,*} Alexey Tiranov,^{1,†} Martin Hayhurst Appel,^{1,‡} Ying Wang,¹ Leonardo Midolo,¹ Sven Scholz,² Andreas D. Wieck,² Arne Ludwig,² Anders Søndberg Sørensen,¹ and Peter Lodahl¹

¹*Center for Hybrid Quantum Networks (Hy-Q), The Niels Bohr Institute, University of Copenhagen, DK-2100 Copenhagen Ø, Denmark*

²*Lehrstuhl für Angewandte Festkörperphysik, Ruhr-Universität Bochum, Universitätsstraße 150, D-44801 Bochum, Germany*

(Dated: July 4, 2023)

The realization of on-chip quantum interfaces between flying photons and solid-state spins is a key building block for quantum-information processors, enabling, e.g., distributed quantum computing, where remote quantum registers are interconnected by flying photons. Self-assembled quantum dots integrated in nanostructures are one of the most promising systems for such an endeavor thanks to their near-unity photon-emitter coupling and fast spontaneous emission rate. Here we demonstrate high-fidelity on-chip entanglement between an incoming photon and a stationary quantum-dot hole spin qubit. The entanglement is induced by sequential scattering of the time-bin encoded photon interleaved with active spin control within a microsecond, two-orders of magnitude faster than those achieved in other solid-state platforms. Conditioning on detection of a reflected photon renders the entanglement fidelity immune to spectral wandering of the emitter. These results represent a major step towards realizing a quantum node capable of interchanging information with flying photons and on-chip quantum logic, as required for quantum networks and quantum repeaters.

In a future quantum network [1], remote quantum nodes could be connected by a large web of entangled photons. Traditionally these photonic states have been generated probabilistically by fusing smaller states, which typically requires an exponential overhead of ancillary photons [2]. The advent of a deterministic quantum interface between light and matter promises to radically change this notion [3]. For such systems, a flying photon is funneled into a nanophotonic structure and interacts efficiently with a quantum emitter that hosts a single spin [4]. Coherent manipulation of the spin state entangles it with the photon, forming the basis for deterministic quantum gates and, e.g., the generation of photonic cluster states for quantum computing [5, 6].

So far, significant progress has been made towards this goal, particularly the realization of spin-photon entanglement [7–14], spin-spin entanglement [13, 15–18], single-photon switching and swap gate [19–21], and photon-photon entanglement [22–24] using various quantum emitters. Among these platforms, quantum dots (QDs) integrated in nanophotonic structures offer near-unity coupling to light ($\beta \geq 98\%$) [25] and a high photon-generation rate with near-unity purity and coherence [26, 27]. Despite proven to be an excellent single-photon source, an interface capable of producing entanglement between a flying photon and the QD has yet to be demonstrated. This approach to entanglement generation is particularly attractive in the context of long-distance quantum communication, as the pulse profile of an incoming photon is preserved upon scattering [28], which unlocks the prospects of interfacing distant emitters [17], realizing one-way quantum repeaters [29], and performing quantum gate operations between two photons [22] or QDs [30].

Here we step forward in this direction by demonstrating high-fidelity spin-photon entanglement between a guided photon and a QD spin embedded in a planar two-sided photonic-crystal waveguide. The entanglement is created in less than a microsecond, by sequential scattering of time-bin encoded photons using a QD heavy-hole spin. Conditioning on the detection of a reflected photon, renders the entanglement fidelity resistant to any residual spectral diffusion intrinsic to the emitter. The protocol can be extended to realize a fully deterministic entangling gate using single-sided waveguides [31].

Results

Concept. The protocol used to induce entanglement between a flying photon and the localized QD spin is outlined in Fig. 1. A single photon pulse is prepared in a superposition of an early $|e\rangle$ and a late $|l\rangle$ time-bin $|\psi_p\rangle = \alpha|e\rangle + \beta|l\rangle$ for $\alpha, \beta \in \mathbb{C}$ constituting a flying qubit. The photon is launched into a waveguide where the embedded QD spin is initialized in $|\psi_s\rangle = |\downarrow\rangle$. The protocol proceeds by alternating between coherent spin rotations \hat{R}_y and single-photon scattering \hat{S} , cf. Fig. 1d. A $\hat{R}_y(\pi/2)$ pulse prepares the spin in a superposition of the two spin ground states $|\downarrow\rangle$ and $|\uparrow\rangle$, while $\hat{R}_y(\pi)$ serves two purposes: (1) to invert the spin in-between the two scattering events to create entanglement, and; (2) to prolong the spin coherence time by acting as a spin-echo pulse between the two equally

* Email to: ming-lai.chan@nbi.ku.dk

† Present address: Chimie ParisTech, Université PSL, CNRS, Institut de Recherche de Chimie Paris, 75005 Paris, France

‡ Present address: Cavendish Laboratory, University of Cambridge, JJ Thomson Avenue, Cambridge, CB3 0HE, UK

long time-bins [32], when the spin is measured in the equatorial basis. \hat{S} corresponds to the photon being reflected (transmitted) when the QD state is in $|\uparrow\rangle$ ($|\downarrow\rangle$) (Fig. 1c). When the flying photon is in an equatorial state, e.g., $\alpha = \beta = \frac{1}{\sqrt{2}}$, the ideal protocol results in the output state

$$\begin{aligned} |\psi_{\text{out}}\rangle &\propto [\alpha |e \downarrow\rangle - \beta |l \uparrow\rangle]_{\mathbf{r}} + [\alpha |e \uparrow\rangle - \beta |l \downarrow\rangle]_{\mathbf{t}} \\ &\equiv |\phi^-\rangle_{\mathbf{r}} + |\psi^-\rangle_{\mathbf{t}}, \end{aligned} \quad (1)$$

which is a superposition of two spatially separated spin-photon Bell states. The subscript \mathbf{r} (\mathbf{t}) indicates that the photon was reflected (transmitted) by the QD. By post-selecting the detection on a photon being reflected (transmitted), the Bell state in the first (second) bracket is prepared. We find that the conditional Bell-state fidelity can approach unity for our system due to the spectral selectivity of the QD that predominantly reflects photons resonant with the transition $|\uparrow\rangle \rightarrow |\uparrow\downarrow\rangle$, despite residual QD spectral diffusion visible from the broadened transmission dip in Fig. 1c (Supplementary Note 4).

Pre-calibration of the QD device. We subdivide the entanglement protocol into two separate experiments (Fig. 2). The first experiment probes the coherent nature of single-photon scattering (Fig. 2a), whereas the second experiment investigates the spin coherence with the built-in spin-echo sequence (Fig. 2c).

Probing single-photon interference. To demonstrate coherent scattering in the single-photon regime, we use a weak coherent state with a mean photon number per pulse $\bar{n} \ll 1$. We prepare a time-bin qubit using an asymmetric Mach-Zehnder interferometer where a photon is superposed between early and late temporal modes $|e\rangle$ and $|l\rangle$, and scatter off the QD spin initialized in $|\uparrow\rangle$. If the input photon of spectral width $\sigma_o/2\pi$ is much narrower than the QD linewidth $\Gamma/2\pi$, the photon can be fully reflected due to destructive interference in transmission [33]. By interfering temporal modes of the reflected photon using the same interferometer and projecting on the X-basis $|\pm X\rangle_p = |e\rangle \pm |l\rangle$, the intensities $I_{\pm X}$ are measured, which are used to estimate the photon visibility $V_p \equiv \frac{I_{+X} - I_{-X}}{I_{+X} + I_{-X}}$. Due to the finite interferometric delay $\tau_{\text{delay}} = 11.8$ ns, fluctuations occurring on longer timescales than τ_{delay} (i.e., spectral diffusion of QDs [34]) are essentially filtered out, as they influence the reflected phase of both time-bins equally. The single-photon interference is thus subject to only fast dephasing processes. Notably, in the single-photon regime ($\bar{n} \approx 0$), we found $V_p = \frac{\Gamma}{\Gamma + 2\gamma_d}$ for the total decay rate $\Gamma \approx 2.48$ ns⁻¹ [14] and γ_d is the pure dephasing rate (Supplementary Note 3). Here we measured a maximum value of $V_p = (89.7 \pm 0.4)\%$ which reduces linearly with \bar{n} (Fig. 2b). Extrapolating a linear fit of V_p to the y -intercept where $\bar{n} = 0$ enables us to extract $\gamma_d \approx (0.099 \pm 0.004)$ ns⁻¹.

Spin-Echo interferometry. The second experiment benchmarks the coherence of the internal hole spin qubit. Specifically, we perform a spin-echo sequence [35] consisting of two $\hat{R}_y(\pi/2)$ pulses separated by a $\hat{R}_y(\pi)$ pulse (Fig. 2c), which are implemented via the two-photon Raman scheme demonstrated in Ref. [36] (see Methods). After the first $\hat{R}_y(\pi/2)$ pulse, due to fluctuating Overhauser nuclear fields [37] the spin state begins to fan out over the Bloch sphere equator (denoted by blue arrows) decaying with a spin dephasing time $T_2^* = 23.2$ ns [14]. Applying a $\hat{R}_y(\pi)$ pulse after time τ inverts the direction of spin precession, thus refocusing the spin state at $t = 2\tau$. The spin coherence is then probed by applying a second $\hat{R}_y(\pi/2)$ pulse, and scanning its phase ϕ_r followed by spin readout, which projects the resulting spin state onto either the optically bright or dark state. The resulting interferometric fringe is depicted in Fig. 2d with an extracted visibility of $V_s = (57.5 \pm 0.4)\%$ at $\tau = 13$ ns, which is primarily limited by photo-induced incoherent spin processes [14]. V_s indicates how well the spin coherence is preserved, and benchmarks the quality of spin-photon correlations on the equatorial basis.

Entanglement generation. Having characterized the coherences of both qubits, we are in a position to run the entanglement protocol. The spin is first prepared in a superposition state $|+X\rangle_s \propto |\uparrow\rangle + |\downarrow\rangle$ by a 3.5 ns $\hat{R}_y(\pi/2)$ pulse (Fig. 3a). The time-bin qubit is attenuated to $\bar{n} \approx 0.09$ before interacting with the QD (Supplementary Note 5). After sequential scattering of each time-bin, the reflected signal is collected and measured by the interferometer. Post-selecting the reflected photonic component carves out the output state [Eq. (1)] resulting in $|\phi^-\rangle_{\mathbf{r}}$ [38].

To determine the fidelity of the entangled state, we perform correlation measurements between the photonic modes and spin states. This involves projecting the entangled state on the $\hat{\sigma}_i^{(p)} \otimes \hat{\sigma}_i^{(s)}$ bases, where $i \in \{x, y, z\}$ denotes the Pauli operator, and the superscripts s (p) represent the spin and photonic qubits. The state of the reflected photon is detected in different time-bin windows after the interferometer, while the spin readout is performed by applying another rotation pulse \hat{R}_i followed by optical driving of the main transition (See Methods; Fig. 3a).

For each experimental setting, we condition on the detection of a reflected photon and the spin readout. The

entanglement fidelity is measured using [14]

$$\mathcal{F}_{\text{Bell}} = \frac{\langle \hat{P}_z \rangle}{2} + \frac{\langle \hat{M}_y \rangle - \langle \hat{M}_x \rangle}{4}, \quad (2)$$

where $\langle \hat{M}_i \rangle = \langle \hat{\sigma}_i^{(p)} \otimes \hat{\sigma}_i^{(s)} \rangle$ is the normalized contrast, and $\langle \hat{P}_z \rangle \equiv (1 + \langle \hat{M}_z \rangle)/2$. For measuring $\langle \hat{M}_{x/y} \rangle$, $\hat{R}_i = \hat{R}_{y/x}(\pi/2)$ is required for spin projection onto the equatorial state. Since the protocol now resembles a spin-echo sequence, the central $\hat{R}_y(\pi)$ pulse has an added benefit of spin-refocusing, whereas for Z-basis projections, spin echo is not necessary as $\langle \hat{P}_z \rangle$ is impervious to spin dephasing. As such, $|\langle \hat{M}_{x/y} \rangle|$ is dictated by the spin-echo visibility V_s , while $\langle \hat{P}_z \rangle$ largely reflects fidelity of the $\hat{R}_y(\pi)$ pulse F_π (Supplementary Note 2). Figures 3b-d show the raw (background corrected) coincidence counts in various readout bases. We record $\langle \hat{P}_z \rangle = (90.7 \pm 2.2)\%$, $\langle \hat{M}_x \rangle = (-58.8 \pm 4.5)\%$ and $\langle \hat{M}_y \rangle = (57.3 \pm 6.6)\%$, where residual background counts from laser rotation pulses were subtracted (Supplementary Note 9). The recorded values of $|\langle \hat{M}_{x/y} \rangle|$ and $\langle \hat{P}_z \rangle$ are consistent with measured V_s and F_π , respectively (see Methods). Using Eq. (2), we obtain a corrected Bell-state fidelity of $\mathcal{F}_{\text{Bell}} = (74.3 \pm 2.3)\%$ (raw fidelity of $(66 \pm 2)\%$), which far exceeds the classical limit of 50%, clearly demonstrating the presence of entanglement in the generated quantum state.

Theoretical modelling. To unravel the physical mechanisms limiting the experimental fidelity, we derive the fidelity (Supplementary Note 2) in the perturbative limit of small errors,

$$\mathcal{F}_{\text{Bell}}^{\text{theory}} \approx 1 - \frac{\gamma_d}{\Gamma} - \frac{\Gamma^2}{4\Delta_h^2}, \quad (3)$$

where Δ_h is the ground-state splitting. Eq. (3) holds in the regime $\gamma_d \ll \Gamma \ll \Delta_h$ and assumes perfect manipulation of the hole spin state. In addition to being resilient to ground-state dephasing due to the built-in spin echo, the protocol is also impervious to errors arising from the spectral mismatch between the incoming optical pulse and the QD transition. This robustness is granted by the QD spectral reflectivity, which sifts out events where the photon interacts with the QD. The off-resonant frequency component of the incident pulse is transmitted without being detected thus having no impact on the entanglement fidelity.

Using Eq. (3) with experimental parameters, the theoretical fidelity is estimated to be $\mathcal{F}_{\text{Bell}}^{\text{theory}} = 96.2\%$. Here the infidelity is attributed to decoherence from elastic phonon scattering [39] γ_d (3.7%) and reflection from the off-resonant spin state Γ/Δ_h (0.1%). The comparison to the experimental result indicates that several additional error mechanisms influence the experiment. The dominant cause is an incoherent photo-induced spin-flip error leading to non-ideal spin rotations, as is visible on the spin-echo data (Fig. 2d). These rotation errors together amount to a total infidelity of 15% (Supplementary Note 2). Additional sources of error originate from driving-induced dephasing due to finite \bar{n} (7.2%) and imperfect spin readout (2.7%), which are not intrinsic to the protocol. Taking these into account we estimate a theoretical lower fidelity bound $\mathcal{F}_{\text{total}}^{\text{theory}} \geq 73.0\%$, which agrees with the experimental value within the error margins. Suppressing the photo-induced incoherent spin-flip processes is essential for improving the fidelity further. Encouragingly spin-rotation fidelities of 98.9% have been realized in the literature on electron spins [36] and could be combined with nuclear-spin cooling methods to realize T_2^* beyond 100 ns [40]. With these improvements a near-unity entanglement fidelity is within reach.

Discussions

The device performance is benchmarked by the entanglement fidelity, protocol speed and generation rate (Supplementary Note 7). In the present work, the demonstrated high entanglement fidelity (74%) is competitive with previous solid-state implementations [41, 42], while the speed is improved. Indeed, the protocol operates on a sub-microsecond timescale (0.6 μs) which is at least 2 orders of magnitude faster than realized in SiV and atomic systems [13, 43, 44] as a consequence of the faster spin preparation time. The realized entanglement rate of 4.7 Hz of the present device can be readily improved by increasing the collection efficiency and reflectivity of the device (Supplementary Note 7).

Since the present implementation is conditioned on the detection of a reflected photon, the overall efficiency is bounded to at most 50%. By adopting a single-sided waveguide or equivalently coupling the incident light to both reflection and transmission ports via a stabilized interferometer, a fully deterministic spin-photon quantum gate [31] can eventually be realized. For a single-sided device all photons are reflected but with a spin-dependent phase. As such, no post-selection is required though the fidelity will be sensitive to spectral drifts of the QD transition to the second order. This however does not pose a fundamental limit to our platform as near-lifetime-limited QD transitions in photonic structures compatible with the proposed scheme were recently reported [45].

We have demonstrated spin-photon entanglement by scattering an incoming photonic qubit off of a stationary QD spin. The system versatility is reflected by the fact that the same QD can also be operated as a source of multi-photon

time-bin encoded entanglement generation [14]. Such versatile spin-photon interfaces constitute building blocks of one-way quantum repeaters [29]. Furthermore, a range of new integrated quantum photonics devices and functionalities could potentially be realized, e.g., a deterministic Bell-state analyzer or a photonic quantum non-demolition detector [31, 46] that both rely on faithful coherent quantum state transfer from a flying photon to an emitter. The reflection-based scheme can be extended to realize non-local quantum entangling gates between distant quantum emitters [17]. Finally, applying the above protocol interleaved with spin rotations in a single-sided device would realize entanglement between two subsequently incoming photons, i.e., a deterministic photon-photon quantum gate [22], which is the most challenging quantum operation in photonics.

Methods

Spin-photon interface. To achieve the highly efficient light-matter interaction required by the protocol, we prepare a QD embedded in a suspended photonic-crystal waveguide (PCW) with two ports (Supplementary Note 1). The p-i-n heterostructure contains an intrinsic layer of self-assembled InAs QDs, enabling the electrical control of the QD charge state by applying a forward bias voltage. One experimental challenge is to simultaneously realize optical cycling transitions and spin control. This was recently achieved with a QD in a PCW under an in-plane magnetic field (Voigt geometry) by exploiting the inherent radiative asymmetry of the PCW [47]. We employ a positively charged exciton giving access to a meta-stable hole spin ground state that was characterized in previous work [47]. An in-plane external magnetic field ($\mathbf{B}_y = 2$ T) Zeeman-splits the QD spin state into four energy levels, see Fig. 1b, where the linearly X- and Y-polarized dipoles form two Λ -systems. Thanks to the optical cyclicity of $C = \gamma_Y/\gamma_X \gg 1$ where the radiative decay rate γ_Y (γ_X) is strongly enhanced (suppressed) by the PCW, an effective two-level system $|\uparrow\rangle \leftrightarrow |\downarrow\downarrow\rangle$ resembling a “QD mirror” is realized. This leads to spin-dependent reflection of photons into the same frequency and polarization modes, granting the spectral selectivity necessary for the entanglement protocol. The relevant system rates and parameters are summarized in Table 1.

Experimental setup. To perform high-fidelity entanglement experiments, the sample chip is cooled to 4.2 K inside a closed-cycle cryostat to suppress phonon scattering. A superconducting vector magnet provides a 2 T in-plane magnetic field enabling Raman transitions between two hole ground states. The sample is imaged with a 0.81 NA objective and brought to focus by translating 3 piezo positioners mounted beneath the sample. A DC voltage source provides a bias voltage at 1.148 V across the sample to populate QD charge states via tunnel coupling to a Fermi reservoir and control the charge environment.

The experiment utilizes the same laser setup as in Ref. [14] with a few notable differences: Two continuous wave (CW) lasers (linewidth < 10 kHz) are used for the creation of the photonic qubit, resonant excitation of the QD and spin rotations. One of which is first directed to a double-pass acousto-optic modulator (AOM) setup followed by an electro-optical modulator (EOM; iXBlue NIR-MX800-LN-20) to generate 2 ns (FWHM) pulses for the photonic qubit. The non-diffracted light from the first AOM setup is then sent to a second AOM setup to create spin initialization and readout pulses (200 ns each) of the same laser frequency. The qubit laser pulses and QD emission are focused and collected at the same grating outcoupler using a cross-polarization scheme (Supplementary Note 1), while the readout laser is coupled directly on top of the QD (Fig. 1a).

A photonic qubit encoded in time-bins is created by passing the 2 ns pulses through an asymmetric Mach-Zehner interferometer with a time delay of $\tau_{\text{delay}} = 11.82$ ns. Here we chose the FWHM duration for the input pulse to be 2 ns which exceeds the radiative lifetime of the optical transition $\Gamma^{-1} = 0.4$ ns for efficient single-photon scattering, but is narrow enough to be fitted within the 11.8 ns time delay when combined with a 7 ns π -rotation pulse and 1 ns rise/fall time. The qubit phase θ_p can be scanned using a quarter-waveplate (QWP) and a linear polarizer. The reflected signal is then reinjected into the same interferometer and subsequently two narrowband (3 GHz) etalon filters to remove background from the rotation laser as well as QD phonon sidebands. The filtered signal then passes through a QWP and an EOM (not shown) which sets a 50/50 splitting ratio on the polarizing beam-splitter (see Fig. 2a). Since both the photonic qubit preparation and readout are performed via the same interferometer, the experiment becomes very robust against any mechanical or thermal drift allowing near-unity interferometric visibility on a week-long timescale [14].

Another CW laser is used for coherent spin control. It is sent through a third AOM setup and another EOM which is amplitude-modulated by a microwave source to create two sidebands with frequency difference matching the ground state splitting $\Delta_h/2\pi = 7.3$ GHz, thus effectively driving the ground-state spin manifold. The sidebands are red-detuned from the cycling transition by 350 GHz to avoid populating the excited states. The phase ϕ_r of the last microwave $\pi/2$ -pulse is induced by a combination of a phase shifter and switches [14] with a phase offset of $\sim 0.3\pi$. The total pulse sequence duration is set to 606 ns.

Spin-photon state projections. As shown in Fig. 3a, the detection of an early (late) photon traversing through the short (long) path of the interferometer constitutes the $\hat{\sigma}_z^{(p)}$ -basis measurement (green). The spin readout in the

$\hat{\sigma}_z^{(s)}$ -basis is performed by applying another rotation pulse $\hat{R}_i = \hat{R}_y(0) (\hat{R}_y(\pi))$ followed by optical driving of the main transition. Similarly, projection on the $\hat{\sigma}_x^{(p)} \otimes \hat{\sigma}_x^{(s)}$ ($\hat{\sigma}_y^{(p)} \otimes \hat{\sigma}_y^{(s)}$) bases is performed by detecting photons in the middle time window (blue) at $\theta_p \approx 2\pi \equiv \theta_0$ ($\theta_p = \theta_0 + \pi/2$) where the early and late time-bins between the short and long paths [14] interfere, followed by $\hat{R}_i = \hat{R}_y(\pm\pi/2)$ ($\hat{R}_x(\pm\pi/2)$) before the spin readout.

Data availability statement The experimental data and analysis scripts of this study are available from the repository: <https://doi.org/10.17894/ucph.3b3bf28d-1f43-4b81-a03d-c9a9d3029b46>.

Acknowledgements

The authors thank Yuxiang Zhang for fruitful discussions. We gratefully acknowledge financial support from Danmarks Grundforskningsfond (DNRF 139, Hy-Q Center for Hybrid Quantum Networks), Styrelsen for Forskning og Innovation (FI) (5072-00016B QUAN-TECH), the European Union’s Horizon 2020 research and innovation programme under grant agreement No. 820445 and project name Quantum Internet Alliance, the European Union’s Horizon 2020 Research and Innovation programme under grant agreement No. 861097 (project name QUDOT-TECH). SS, ADW and AL gratefully acknowledge financial support from Deutsche Forschungsgemeinschaft (DFG) (TRR 160 and LU2051/1-1) and the grants QR.X 16KISQ009 and DFH/UFA CDFA-05-06.

Competing interests P.L. is founder of the company Sparrow Quantum that commercializes single-photon sources. The remaining authors declare no competing interests.

Author Contributions

M.L.C. and A.T. contributed equally to this work. M.L.C. and A.T. performed the experiment, and theoretical analysis with help from A.S.S. Y.W. fabricated the device. A.L. and S.S. performed the heterostructure wafer growth with input from A.D.W. M.L.C. and A.T. analyzed the data with help from M.H.A. M.L.C., A.T., and P.L. wrote the manuscript with input from all authors. P.L., A.S.S., L.M., A.L., and A.D.W. supervised the project.

-
- [1] Briegel, H. J., Browne, D. E., Dür, W., Raussendorf, R. & Van den Nest, M. Measurement-based quantum computation. *Nature Physics* **5**, 19–26 (2009).
 - [2] Browne, D. E. & Rudolph, T. Resource-efficient linear optical quantum computation. *Phys. Rev. Lett.* **95**, 010501 (2005).
 - [3] Uppu, R., Midolo, L., Zhou, X., Carolan, J. & Lodahl, P. Quantum-dot-based deterministic photon–emitter interfaces for scalable photonic quantum technology. *Nature Nanotechnology* **16**, 1308–1317 (2021).
 - [4] Lodahl, P., Ludwig, A. & Warburton, R. J. A deterministic source of single photons. *Physics Today* **75**, 44–50 (2022).
 - [5] Lindner, N. H. & Rudolph, T. Proposal for pulsed on-demand sources of photonic cluster state strings. *Phys. Rev. Lett.* **103**, 113602 (2009).
 - [6] Pichler, H., Choi, S., Zoller, P. & Lukin, M. D. Universal photonic quantum computation via time-delayed feedback. *Proceedings of the National Academy of Sciences* **114**, 11362–11367 (2017).
 - [7] Togan, E. *et al.* Quantum entanglement between an optical photon and a solid-state spin qubit. *Nature* **466**, 730–734 (2010).
 - [8] Gao, W. B., Fallahi, P., Togan, E., Miguel-Sanchez, J. & Imamoglu, A. Observation of entanglement between a quantum dot spin and a single photon. *Nature* **491**, 426–430 (2012).
 - [9] De Greve, K. *et al.* Complete tomography of a high-fidelity solid-state entangled spin–photon qubit pair. *Nature Communications* **4**, 2228 (2013).
 - [10] Schaibley, J. R. *et al.* Demonstration of quantum entanglement between a single electron spin confined to an inas quantum dot and a photon. *Phys. Rev. Lett.* **110**, 167401 (2013).
 - [11] Schwartz, I. *et al.* Deterministic generation of a cluster state of entangled photons. *Science* **354**, 434–437 (2016).
 - [12] He, Y. *et al.* Quantum state transfer from a single photon to a distant quantum-dot electron spin. *Phys. Rev. Lett.* **119**, 060501 (2017).
 - [13] Nguyen, C. T. *et al.* Quantum network nodes based on diamond qubits with an efficient nanophotonic interface. *Phys. Rev. Lett.* **123**, 183602 (2019).
 - [14] Appel, M. H. *et al.* Entangling a hole spin with a time-bin photon: A waveguide approach for quantum dot sources of multiphoton entanglement. *Phys. Rev. Lett.* **128**, 233602 (2022).
 - [15] Delteil, A. *et al.* Generation of heralded entanglement between distant hole spins. *Nature Physics* **12**, 218–223 (2016).
 - [16] Stockill, R. *et al.* Phase-tuned entangled state generation between distant spin qubits. *Phys. Rev. Lett.* **119**, 010503 (2017).
 - [17] Daiss, S. *et al.* A quantum-logic gate between distant quantum-network modules. *Science* **371**, 614–617 (2021).
 - [18] Dordevic, T. *et al.* Entanglement transport and a nanophotonic interface for atoms in optical tweezers. *Science* **373**, 1511–1514 (2021).

- [19] Sun, S., Kim, H., Luo, Z., Solomon, G. S. & Waks, E. A single-photon switch and transistor enabled by a solid-state quantum memory. *Science* **361**, 57–60 (2018).
- [20] Javadi, A. *et al.* Spin–photon interface and spin-controlled photon switching in a nanobeam waveguide. *Nature Nanotechnology* **13**, 398–403 (2018).
- [21] Bechler, O. *et al.* A passive photon–atom qubit swap operation. *Nature Physics* **14**, 996–1000 (2018).
- [22] Hacker, B., Welte, S., Rempe, G. & Ritter, S. A photon–photon quantum gate based on a single atom in an optical resonator. *Nature* **536**, 193–196 (2016).
- [23] Istrati, D. *et al.* Sequential generation of linear cluster states from a single photon emitter. *Nature Communications* **11**, 5501 (2020).
- [24] Thomas, P., Ruscio, L., Morin, O. & Rempe, G. Efficient generation of entangled multiphoton graph states from a single atom. *Nature* **608**, 677–681 (2022).
- [25] Arcari, M. *et al.* Near-unity coupling efficiency of a quantum emitter to a photonic crystal waveguide. *Phys. Rev. Lett.* **113**, 093603 (2014).
- [26] Tomm, N. *et al.* A bright and fast source of coherent single photons. *Nature Nanotechnology* **16**, 399–403 (2021).
- [27] Uppu, R. *et al.* Scalable integrated single-photon source. *Science Advances* **6**, eabc8268 (2020).
- [28] Duan, L.-M. & Kimble, H. J. Scalable photonic quantum computation through cavity-assisted interactions. *Phys. Rev. Lett.* **92**, 127902 (2004).
- [29] Borregaard, J. *et al.* One-way quantum repeater based on near-deterministic photon-emitter interfaces. *Phys. Rev. X* **10**, 021071 (2020).
- [30] Mahmoodian, S., Lodahl, P. & Sørensen, A. S. Quantum networks with chiral-light–matter interaction in waveguides. *Phys. Rev. Lett.* **117**, 240501 (2016).
- [31] Borregaard, J., Sørensen, A. S. & Lodahl, P. Quantum networks with deterministic spin–photon interfaces. *Advanced Quantum Technologies* **2**, 1800091 (2019).
- [32] Tiurev, K. *et al.* High-fidelity multiphoton-entangled cluster state with solid-state quantum emitters in photonic nanostructures. *Phys. Rev. A* **105**, L030601 (2022).
- [33] Shen, J. T. & Fan, S. Coherent photon transport from spontaneous emission in one-dimensional waveguides. *Opt. Lett.* **30**, 2001–2003 (2005).
- [34] Kuhlmann, A. V. *et al.* Charge noise and spin noise in a semiconductor quantum device. *Nature Physics* **9**, 570–575 (2013).
- [35] Hahn, E. L. Spin echoes. *Phys. Rev.* **80**, 580–594 (1950).
- [36] Bodey, J. H. *et al.* Optical spin locking of a solid-state qubit. *npj Quantum Information* **5**, 95 (2019).
- [37] Urbaszek, B. *et al.* Nuclear spin physics in quantum dots: An optical investigation. *Rev. Mod. Phys.* **85**, 79–133 (2013).
- [38] Welte, S., Hacker, B., Daiss, S., Ritter, S. & Rempe, G. Cavity carving of atomic bell states. *Phys. Rev. Lett.* **118**, 210503 (2017).
- [39] Tighineanu, P., Dreeßen, C. L., Flindt, C., Lodahl, P. & Sørensen, A. S. Phonon decoherence of quantum dots in photonic structures: Broadening of the zero-phonon line and the role of dimensionality. *Phys. Rev. Lett.* **120**, 257401 (2018).
- [40] Jackson, D. M. *et al.* Optimal purification of a spin ensemble by quantum-algorithmic feedback. *Phys. Rev. X* **12**, 031014 (2022).
- [41] Tchebotareva, A. *et al.* Entanglement between a diamond spin qubit and a photonic time-bin qubit at telecom wavelength. *Phys. Rev. Lett.* **123**, 063601 (2019).
- [42] Kim, H., Bose, R., Shen, T. C., Solomon, G. S. & Waks, E. A quantum logic gate between a solid-state quantum bit and a photon. *Nature Photonics* **7**, 373–377 (2013).
- [43] Bhaskar, M. K. *et al.* Experimental demonstration of memory-enhanced quantum communication. *Nature* **580**, 60–64 (2020).
- [44] Kalb, N., Reiserer, A., Ritter, S. & Rempe, G. Heralded storage of a photonic quantum bit in a single atom. *Phys. Rev. Lett.* **114**, 220501 (2015).
- [45] Pedersen, F. T. *et al.* Near transform-limited quantum dot linewidths in a broadband photonic crystal waveguide. *ACS Photonics* **7**, 2343–2349 (2020).
- [46] Witthaut, D., Lukin, M. D. & Sørensen, A. S. Photon sorters and QND detectors using single photon emitters. *EPL (Europhysics Letters)* **97**, 50007 (2012).
- [47] Appel, M. H. *et al.* Coherent spin-photon interface with waveguide induced cycling transitions. *Phys. Rev. Lett.* **126**, 013602 (2021).

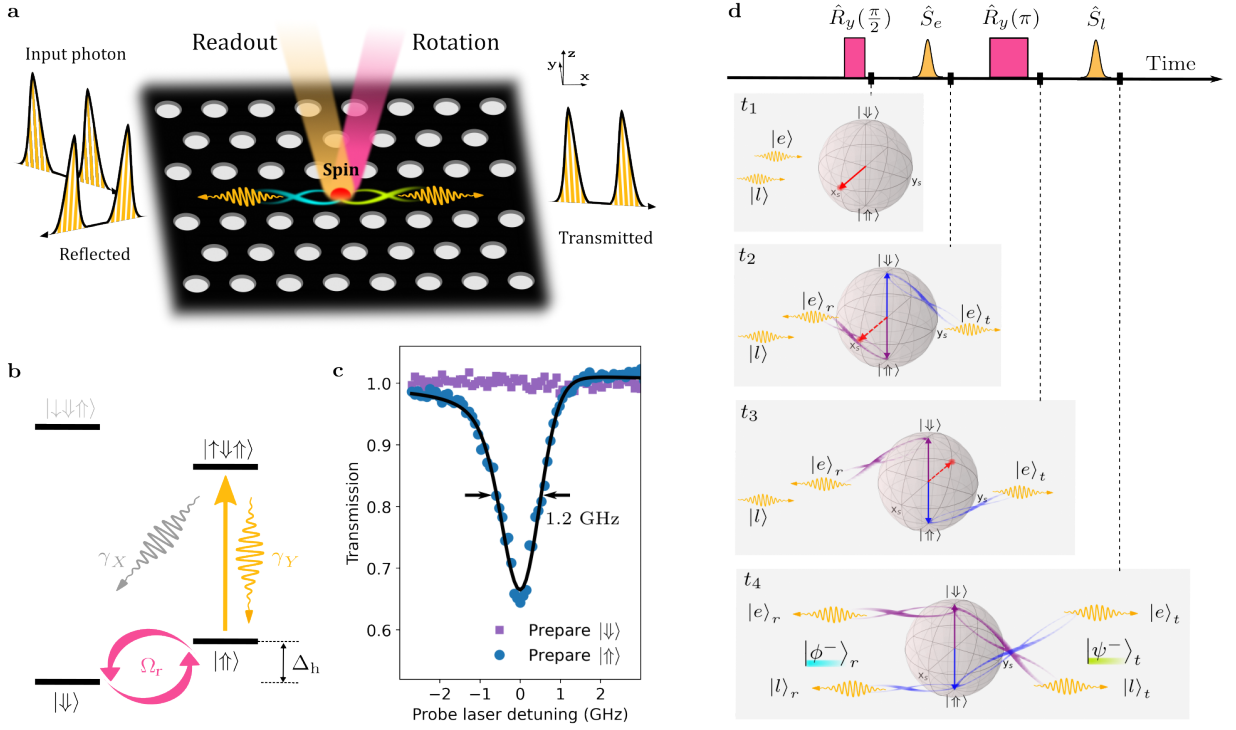


FIG. 1. **Generation protocol of on-chip spin-photon entanglement.** (a) A coherently controlled spin in a QD (red) inside a photonic-crystal waveguide, where a Bell state (cyan lines) is generated upon conditional detection of a reflected photon. (b) QD level diagram. The excited state $|\uparrow\downarrow\uparrow\rangle$ predominantly decays into $|\uparrow\uparrow\rangle$ with rate γ_Y as $\gamma_Y \gg \gamma_X$. The wavelength of the main transition is 945 nm. Coherent control of the metastable hole spin ground states (magenta arrows, Rabi frequency Ω_r) is realized via two-photon Raman processes by a detuned laser. (c) Single-photon transmission spectrum of the QD at $\mathbf{B}_y = 2$ T when preparing the spin state in either $|\uparrow\uparrow\rangle$ or $|\downarrow\downarrow\rangle$. (d) State evolution at different points in time during the protocol. At t_1 , the QD spin (red) is prepared in a superposition state. At t_2 , spin-dependent QD scattering occurs for the early time-bin $|e\rangle$. A π -rotation of the spin at t_3 is followed by scattering of the late time-bin $|l\rangle$ photon pulse at t_4 . The two distinct Bell states $|\phi^-\rangle$ ($|\psi^-\rangle$) are generated conditioned on the detection of a reflected (transmitted) photon.

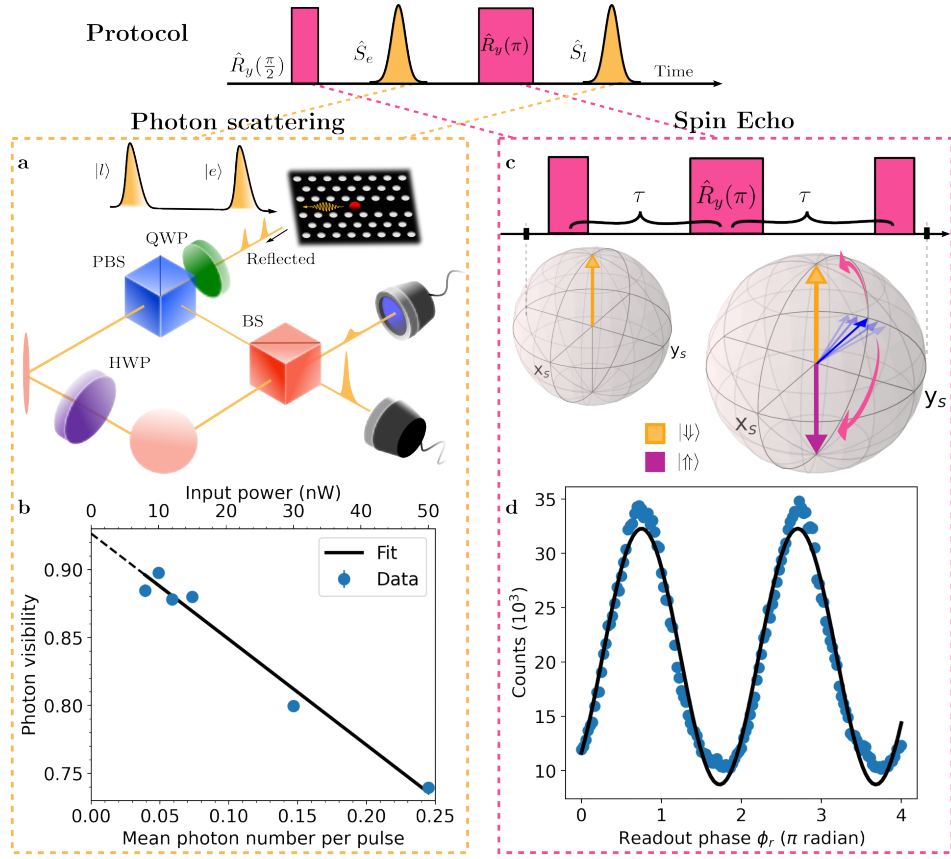


FIG. 2. **Coherent single-photon scattering and spin control.** (a) Setup for measuring photon visibility. The time-bin encoded qubit is reflected off the QD, which is initialized in the $|\uparrow\rangle$ state. Upon entering the interferometer, the early time-bin is delayed which interferes with the late time-bin, constituting a $|\pm X\rangle_p = |e\rangle \pm |l\rangle$ basis measurement. PBS, polarizing beam-splitter; BS, 50:50 beam-splitter; QWP (HWP), quarter (half) wave-plate. (b) Intensity visibility in photonic X-bases as a function of the mean photon number per pulse \bar{n} . The pure dephasing rate γ_d is extracted from the y -intercept where $\bar{n} = 0$. (c) Spin-echo sequence used to probe the spin coherence. The π -pulse is equally distant from the two $\pi/2$ pulses to eliminate inhomogeneous spin dephasing. The phase of the last $\pi/2$ pulse ϕ_r maps the equatorial state $|\uparrow\rangle + e^{i\phi_r}|\downarrow\rangle$ to the optically bright state $|\uparrow\rangle$ ($\phi_r = \pi$) or dark state $|\downarrow\rangle$ ($\phi_r = 0$). (d) Contrast between the spin $|\downarrow\rangle$ and $|\uparrow\rangle$ populations as a function of ϕ_r .

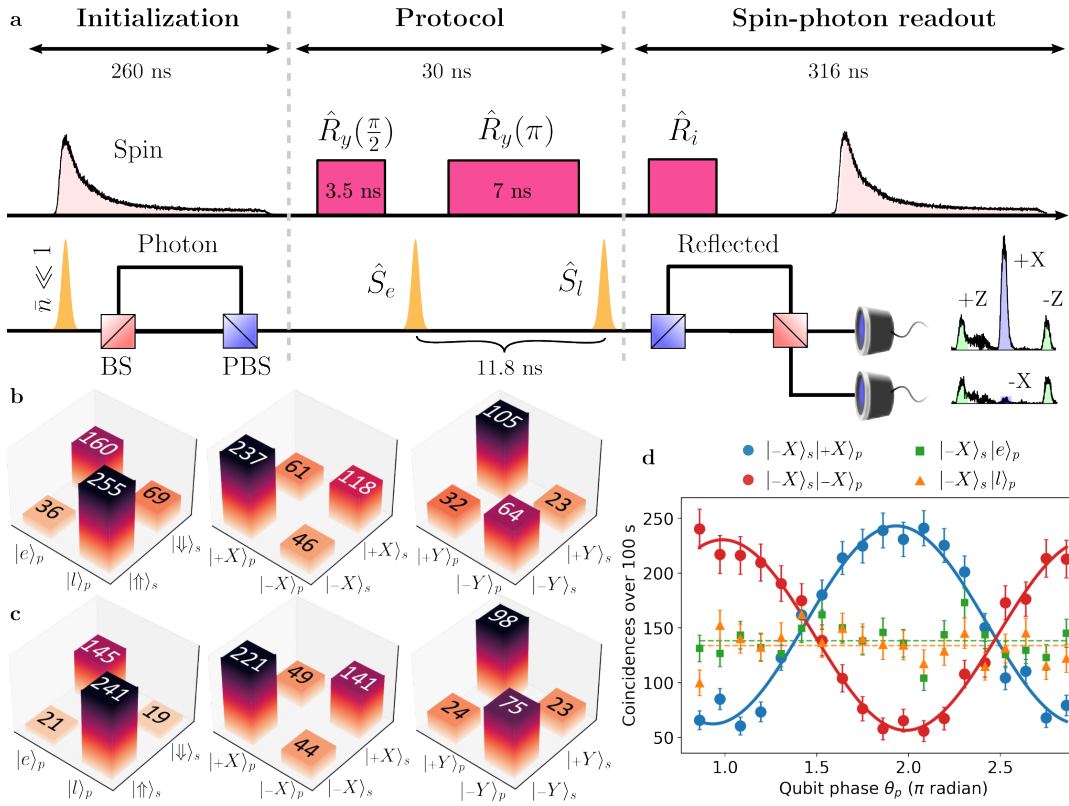


FIG. 3. **Generation and verification of Bell states.** (a) Experimental sequence consisting of the preparation of spin and photonic qubits, the entanglement protocol and readout. The spin state is initialized and read out by optically driving the $|\uparrow\rangle \leftrightarrow |\downarrow\rangle$ transition (pale red), and \hat{R}_i controls the spin projection basis. The photonic qubit is prepared and measured by the same interferometer in either the Z-basis (green) or equatorial basis (blue) time window. (b) Raw two-photon coincidences measured during the photonic (p) readout window and spin (s) projections. (c) Measured two-photon coincidences corrected for laser background. (d) Visibility fringes of background-corrected two-photon coincidences as a function of the qubit phase θ_p when the spin state is projected on $|-\rangle_s \propto |\uparrow\rangle - |\downarrow\rangle$. Circles (squares/triangles) correspond to projection on the photonic X-basis ($\pm Z$ -basis). Solid curves are fits using $V_s \cos(\theta_p + \theta_{\text{offset}})$, and dashed lines are horizontal line fits.

Supplementary Material for “On-chip Spin-Photon Entanglement based on Photon-scattering of a Quantum Dot”

Ming Lai Chan,^{1,*} Alexey Tiranov,^{1,†} Martin Hayhurst Appel,^{1,‡} Ying Wang,¹ Leonardo Midolo,¹ Sven Scholz,² Andreas D. Wieck,² Arne Ludwig,² Anders Søndberg Sørensen,¹ and Peter Lodahl¹

¹*Center for Hybrid Quantum Networks (Hy-Q), The Niels Bohr Institute, University of Copenhagen, DK-2100 Copenhagen Ø, Denmark*

²*Lehrstuhl für Angewandte Festkörperphysik, Ruhr-Universität Bochum, Universitätsstraße 150, D-44801 Bochum, Germany*

CONTENTS

Supplementary Note 1: Cross-polarization Scheme on Waveguides	2
Supplementary Note 2: Theory of Spin-photon Bell State Generation with Single-photon Scattering	3
A. Scattering Coefficients for a Λ -level Emitter in Two-sided Waveguides	4
B. Projection Operators for Measuring Time-bin Encoded Photons	5
C. Formula for the Operational Fidelity	5
D. Perturbative Form of the Entanglement Fidelity	6
1. Spectral mode mismatch	6
2. Finite cyclicity and coupling loss	7
3. Phonon-induced pure dephasing	7
4. Spin dephasing	8
5. Incoherent spin-flip error and finite T_2^*	9
6. Spin readout error	11
7. Driving-induced dephasing due to multi-photon scattering	12
E. Estimate the Overall Entanglement Fidelity	13
Supplementary Note 3: Photon Visibility and Pure Dephasing Rate Estimation	14
Supplementary Note 4: Two-color Transmission Experiment	15
Supplementary Note 5: Spin-dependent Reflectivity Measurement	17
Supplementary Note 6: Optical Spin Control and Rotation Fidelity	19
Principle of Optical Spin Control	19
Measured Spin Rabi Oscillations	19
Supplementary Note 7: Protocol Performance Metrics	21
Supplementary Note 8: Concurrence Estimate	22
Supplementary Note 9: Fidelity Background Subtraction	22
Supplementary References	23

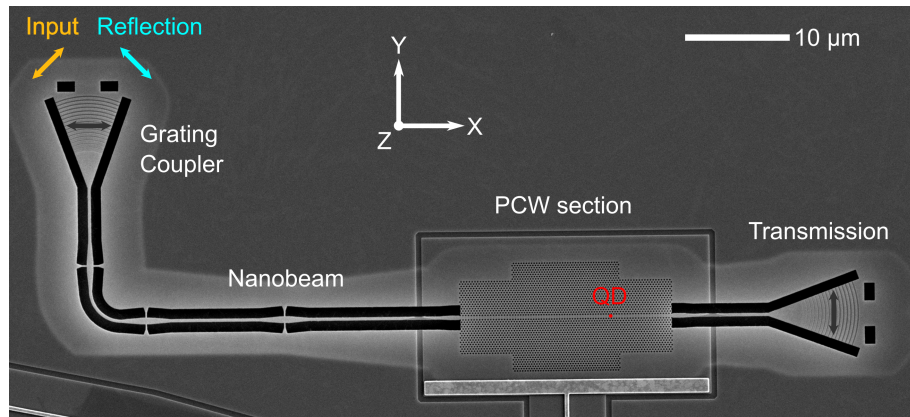
* Email to: ming-lai.chan@nbi.ku.dk; M.L.C. and A.T. contributed equally to this work.

† Present address: Chimie ParisTech, Université PSL, CNRS, Institut de Recherche de Chimie Paris, 75005 Paris, France

‡ Present address: Cavendish Laboratory, University of Cambridge, JJ Thomson Avenue, Cambridge, CB3 0HE, UK

SUPPLEMENTARY NOTE 1: CROSS-POLARIZATION SCHEME ON WAVEGUIDES

The waveguide device used in the current experiment is terminated by two high-efficiency grating outcouplers [1] representing reflection and transmission ports. For implementing the scattering experiment, both the incident laser and reflected signal are coupled to the same grating outcoupler (Supplementary Figure 1). To distinguish the signal from the laser background, a cross-polarized scheme is used for excitation and collection. Before entering the waveguide, the polarization of the input light is carefully optimized with a set of waveplates such that it is orthogonal to the polarization of the collected light (set by another set of waveplates on the optical setup). The input is diagonally polarized (which can also be circularly polarized), thus only 50% of the light is coupled to the grating coupler which has a predefined polarization along X [1]. The X-polarized light is then converted into Y-polarization via the bend in the waveguide and subsequently interacts with the QD. Due to the non-chiral coupling of the waveguide, 50% of the scattered signal thus returns to the same grating coupler, and further passes through the polarization control on the collection path resulting in another 50% loss. Despite the loss in efficiency, the signal-to-noise ratio achieved in this setup can reach $\sim 100\text{-}300$ depending on the mechanical stability of the optical setup. The transmission port constitutes a second collection path which can be used for both resonant transmission and entanglement experiments.



Supplementary Figure 1. Scanning Electron Microscope (SEM) image of the waveguide and polarizations of the input and reflected light. Dark grey arrows denote the predefined polarizations of the grating couplers.

SUPPLEMENTARY NOTE 2: THEORY OF SPIN-PHOTON BELL STATE GENERATION WITH SINGLE-PHOTON SCATTERING

In this section, we discuss the state evolution of the spin-photon system upon applying the entanglement protocol and develop an analytical expression for the entanglement fidelity. Our strategy is similar to the approach taken in Ref. [2], which is to first evaluate the fidelity to lowest order in perturbation theory for each of the considered errors. In the end the full fidelity is then found by multiplying the individual fidelities.

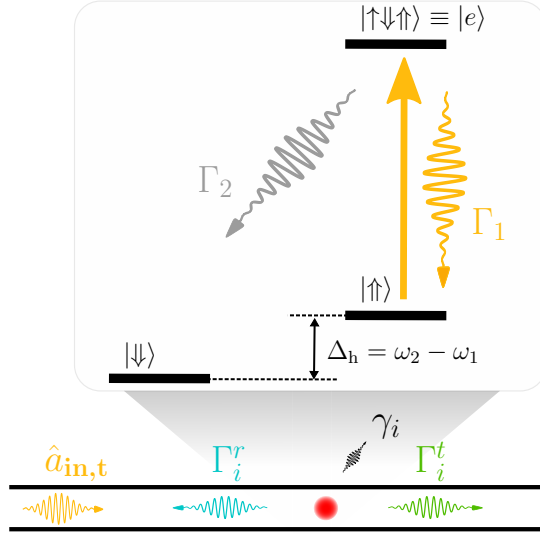
We start with modeling a right-propagating time-bin photonic qubit $\alpha|e\rangle + \beta|l\rangle$ in a two-sided waveguide where $\alpha, \beta \in \mathbb{C}$, and the QD spin is initially in the ground state $|\Downarrow\rangle$. Following from Figure 1d of the main text, the entanglement protocol consists of (1) applying a $\hat{R}_y(\pi/2)$ spin rotation to prepare a superposition spin qubit, (2) scattering of the early photon \hat{S}_e , (3) a $\hat{R}_y(\pi)$ -rotation, and finally (4) the scattering of the late photon \hat{S}_l . Each single-photon scattering process obeys the input-output relations [3]:

$$\begin{aligned}
 \underbrace{|\omega \uparrow\rangle}_{\text{resonant}} &\rightarrow r_1 |\omega \uparrow\rangle_r + t_1 |\omega \uparrow\rangle_t + r_2 |\omega_2 \Downarrow\rangle_r + t_2 |\omega_2 \Downarrow\rangle_t; \\
 \underbrace{|\omega \Downarrow\rangle}_{\text{off-resonant}} &\rightarrow \underbrace{\hat{r}_1 |\omega \Downarrow\rangle_r}_{\text{reflection, left-propagating}} + \underbrace{\hat{t}_1 |\omega \Downarrow\rangle_t}_{\text{transmission, right-propagating}} + \underbrace{\hat{r}_2 |\omega - \Delta_h \uparrow\rangle_r}_{\text{reflection, left, spin-flip}} + \underbrace{\hat{t}_2 |\omega - \Delta_h \uparrow\rangle_t}_{\text{transmission, right, spin-flip}},
 \end{aligned} \tag{1}$$

where the photon in each time-bin is assumed to center around the resonant frequency of the dominant transition ($|\uparrow\rangle \leftrightarrow |\uparrow\Downarrow\rangle$) with a Gaussian spectral profile, and r_1 (t_1) are the reflection (transmission) operators associated with the QD vertical transition $|\uparrow\rangle \rightarrow |\uparrow\Downarrow\rangle$ with a decay rate Γ_1 (γ_Y in the main text). r_2 (t_2) corresponds to the diagonal transition $|\Downarrow\rangle \rightarrow |\uparrow\Downarrow\rangle$ with decay rate Γ_2 ($\equiv \gamma_X$). $\omega_2 = \omega + \Delta_h$ is the frequency of the Raman photon emitted from the diagonal transition where Δ_h is the ground-state splitting. The symbol \circ denotes off-resonant scattering when the spin is in $|\Downarrow\rangle$. Below we use the superscript prime ($'$) to represent a scattered photon of frequency $\omega_2 \neq \omega$. Using Eq. (1), the state evolution of the spin-photon system proceeds as

$$\begin{aligned}
 &\left(\alpha|e\rangle + \beta|l\rangle \right) \otimes |\Downarrow\rangle \xrightarrow{\hat{R}_y(\frac{\pi}{2})} \left(\alpha|e\rangle + \beta|l\rangle \right) \otimes \left(|\uparrow\rangle + |\Downarrow\rangle \right) / \sqrt{2} \\
 &\xrightarrow{\hat{S}_e} \left[\alpha \left(r_1^e |e \uparrow\rangle_r + t_1^e |e \uparrow\rangle_t + r_2^e |e' \Downarrow\rangle_r + t_2^e |e' \Downarrow\rangle_t \right) \right. \\
 &\quad \left. + \alpha \left(\hat{r}_1^e |e \Downarrow\rangle_r + \hat{t}_1^e |e \Downarrow\rangle_t + \hat{r}_2^e |e' \uparrow\rangle_r + \hat{t}_2^e |e' \uparrow\rangle_t \right) + \beta |l \uparrow\rangle + \beta |l \Downarrow\rangle \right] / \sqrt{2} \\
 &\xrightarrow{\hat{R}_y(\pi)} \left[\alpha \left(-r_1^e |e \Downarrow\rangle_r - t_1^e |e \Downarrow\rangle_t + r_2^e |e' \uparrow\rangle_r + t_2^e |e' \uparrow\rangle_t \right) \right. \\
 &\quad \left. + \alpha \left(\hat{r}_1^e |e \uparrow\rangle_r + \hat{t}_1^e |e \uparrow\rangle_t - \hat{r}_2^e |e' \Downarrow\rangle_r - \hat{t}_2^e |e' \Downarrow\rangle_t \right) - \beta |l \Downarrow\rangle + \beta |l \uparrow\rangle \right] / \sqrt{2} \\
 &\xrightarrow{\hat{S}_l} \left[\alpha \left(-r_1^e |e \Downarrow\rangle_r - t_1^e |e \Downarrow\rangle_t + r_2^e |e' \uparrow\rangle_r + t_2^e |e' \uparrow\rangle_t \right) \right. \\
 &\quad \left. + \alpha \left(\hat{r}_1^e |e \uparrow\rangle_r + \hat{t}_1^e |e \uparrow\rangle_t - \hat{r}_2^e |e' \Downarrow\rangle_r - \hat{t}_2^e |e' \Downarrow\rangle_t \right) \right. \\
 &\quad \left. + \beta \left(r_1^l |l \uparrow\rangle_r + t_1^l |l \uparrow\rangle_t + r_2^l |l' \Downarrow\rangle_r + t_2^l |l' \Downarrow\rangle_t \right) \right. \\
 &\quad \left. - \beta \left(\hat{r}_1^l |l \Downarrow\rangle_r + \hat{t}_1^l |l \Downarrow\rangle_t + \hat{r}_2^l |l' \uparrow\rangle_r + \hat{t}_2^l |l' \uparrow\rangle_t \right) \right] / \sqrt{2} = |\psi_{\text{out}}\rangle.
 \end{aligned} \tag{2}$$

In the ideal scenario where the early and late pulses are identical, monochromatic and resonant, and the QD optical cyclicity is infinite with no dephasing and loss, we have: (1) $r_1 \rightarrow -1$ (resonant photons are coherently reflected with a π -phase shift), (2) $\hat{t}_1 \rightarrow 1, \hat{r}_1 \rightarrow 0$ (off-resonant photons are being transmitted instead of reflected), (3) $t_1 \rightarrow 0$ (complete destructive interference in the transmission); and (4) $r_2, \hat{r}_2, t_2, \hat{t}_2 \rightarrow 0$ (there are no Raman photons in the reflected and transmitted modes due to high cyclicity). As such, the ideal output state becomes $[\alpha|e \Downarrow\rangle - \beta|l \uparrow\rangle]_r + [\alpha|e \uparrow\rangle - \beta|l \Downarrow\rangle]_t$. By preparing an equatorial photonic qubit $|\alpha| = |\beta| = \frac{1}{\sqrt{2}}$ and varying its phase θ_p where $\beta/\alpha = e^{i\theta_p}$, all 4 different Bell states can be generated upon conditioning on either the reflection or transmission of a scattered photon.



Supplementary Figure 2. Level scheme for a QD embedded in a two-sided waveguide under the Voigt magnetic field. Γ_1 (Γ_2) is the radiative decay rate into the waveguide from the transition $|e\rangle \rightarrow |\uparrow\rangle$ ($|e\rangle \rightarrow |\downarrow\rangle$). $\Gamma_i = \Gamma_i^t + \Gamma_i^r$ for $i \in \{1, 2\}$ includes both decay rates into the transmitted (“t”) and reflected (“r”) waveguide modes. γ_i is the radiative rate into the lossy modes (Not to be confused with the radiative decay rates $\gamma_Y \equiv \Gamma_1$ and $\gamma_X \equiv \Gamma_2$ in the main text).

A. Scattering Coefficients for a Λ -level Emitter in Two-sided Waveguides

The scattering problem of a weak coherent state on the Λ -level emitter has been solved in Ref. [4] and its formalism can be easily extended to directly compute the scattering coefficients in Eq. (1). Specifically, the output field bosonic operator of the waveguide can be expressed in terms of the incident field and dynamical response of the emitter from the non-Hermitian Hamiltonian $\hat{\mathcal{H}}_{nh}$ [2]. In a two-sided waveguide configuration, we label the field operator in the reflection port by the subscript “r”, and the transmitted port by “t” (Supplementary Figure 2). Assuming that a right-propagating light field $\hat{a}_{in,t}^\dagger$ enters the waveguide, the output field operators on the transmitted (t) and reflected (r) ports are

$$\begin{aligned}
 |\omega \uparrow\rangle : & \begin{cases} \hat{a}_{out,t} = \left[1 - \frac{2\Gamma_1^t}{\Gamma + 2i\delta_1} \hat{\sigma}_{11} - \frac{2\sqrt{\Gamma_1^t \Gamma_2^t}}{\Gamma + 2i\delta_1} \hat{\sigma}_{12} \right] \hat{a}_{in,t} \\ \hat{a}_{out,r} = \left[-\frac{2\sqrt{\Gamma_1^t \Gamma_1^r}}{\Gamma + 2i\delta_1} \hat{\sigma}_{11} - \frac{2\sqrt{\Gamma_1^t \Gamma_2^r}}{\Gamma + 2i\delta_1} \hat{\sigma}_{12} \right] \hat{a}_{in,t} \end{cases} \\
 |\omega \downarrow\rangle : & \begin{cases} \hat{a}_{out,t} = \left[1 - \frac{2\Gamma_1^t}{\Gamma + 2i(\delta_1 + \Delta_h)} \hat{\sigma}_{11} - \frac{2\sqrt{\Gamma_1^t \Gamma_2^t}}{\Gamma + 2i(\delta_1 + \Delta_h)} \hat{\sigma}_{12} \right] \hat{a}_{in,t} \\ \hat{a}_{out,r} = \left[-\frac{2\sqrt{\Gamma_1^t \Gamma_1^r}}{\Gamma + 2i(\delta_1 + \Delta_h)} \hat{\sigma}_{11} - \frac{2\sqrt{\Gamma_1^t \Gamma_2^r}}{\Gamma + 2i(\delta_1 + \Delta_h)} \hat{\sigma}_{12} \right] \hat{a}_{in,t}, \end{cases} \quad (3)
 \end{aligned}$$

where $\delta_1 = \omega_1 - \omega$ is the laser detuning from the transition $|\uparrow\rangle \rightarrow |e\rangle$ for an emitter initialized in $|\uparrow\rangle$. The total decay rate $\Gamma = \Gamma_1 + \Gamma_2 + \gamma_1 + \gamma_2$ where Γ_i (γ_i) is the radiative decay rate into (out of) the waveguide. $\Gamma_i = \Gamma_i^t + \Gamma_i^r$ includes both decay rates into the transmitted (“t”) and reflected (“r”) waveguide modes. Δ_h is the ground-state splitting. The output field operators have different detunings in their denominators because of different initial spin states of the QD: If the spin is initially $|\uparrow\rangle$, the resonant frequency is ω_1 ; If it is $|\downarrow\rangle$ then the resonant frequency required to drive the diagonal spin transition is $\omega_2 = \omega_1 + \Delta_h$. $\hat{\sigma}_{ij} = |j\rangle \langle i|$ is the atomic operator denoting a spin-flip in the atomic state when $i \neq j$. Note that when evaluating the probability of a spin-photon state, i.e., $|e \downarrow\rangle_r$, the corresponding scattering coefficient $r_1^e(\omega)$ is first convoluted with a Gaussian lineshape $\Phi_1(\omega)$ and integrated with respect to ω [2]. The individual resonant scattering coefficients in the frequency domain are

$$t_1(\omega) = 1 - \frac{2\Gamma_1^t}{\Gamma + 2i\delta_1}, \quad t_2(\omega) = -\frac{2\sqrt{\Gamma_1^t \Gamma_2^t}}{\Gamma + 2i\delta_1}, \quad r_1(\omega) = -\frac{2\sqrt{\Gamma_1^t \Gamma_1^r}}{\Gamma + 2i\delta_1}, \quad r_2(\omega) = -\frac{2\sqrt{\Gamma_1^t \Gamma_2^r}}{\Gamma + 2i\delta_1}, \quad (4)$$

where the off-resonant scattering coefficients are found similarly by replacing $\delta_1 \rightarrow \delta_1 + \Delta_h$.

B. Projection Operators for Measuring Time-bin Encoded Photons

At the end of the entanglement protocol, measurements to read out the state of the photonic qubit are performed by registering detector clicks in three different detection time windows. The detection of a time-bin photon is formulated by projection operators on different photonic readout bases:

$$|e\rangle\langle e| = \int_{-\infty}^{\infty} \hat{a}_e^\dagger(t)\hat{a}_e(t)dt, \quad |l\rangle\langle l| = \int_{-\infty}^{\infty} \hat{a}_e^\dagger(t+\tau)\hat{a}_e(t+\tau)dt, \quad |e\rangle\langle l| = \int_{-\infty}^{\infty} \hat{a}_e^\dagger(t)\hat{a}_e(t+\tau)dt = (|l\rangle\langle e|)^\dagger, \quad (5)$$

where the bosonic creation operator $\hat{a}_e^\dagger(t)$ represents the emission of a photon at time t in the early time-bin, and τ is the interferometric delay. The projections $|e\rangle\langle e|$ ($|l\rangle\langle l|$) correspond to detecting photons in the side peak windows (green) (Figure 3a in the main text), whereas $|e\rangle\langle l|$ refers to projection onto the middle detection window (blue central peak) where the early and late photons interfere. Since we only resolve the time-bin, the creation operator can be expressed in either the time or frequency domain. Using $a(t) = \frac{1}{\sqrt{2\pi}} \int_{-\infty}^{\infty} a(\omega)e^{i\omega t}d\omega$, one can show

$$\int_{-\infty}^{\infty} \hat{a}_e^\dagger(t)a_e(t)dt = \int_{-\infty}^{\infty} \hat{a}_e^\dagger(\omega)a_e(\omega)d\omega. \quad (6)$$

This implies we can adopt the same perturbation theory in the frequency domain to evaluate the fidelity as in Ref. [2].

C. Formula for the Operational Fidelity

Now, with the time-bin projection operators defined, we can express the entanglement fidelity in terms of the above scattering coefficients. The measure of the quality of generated quantum states is conventionally given by the fidelity, which in our case evaluates the overlap between the output and ideal Bell states:

$$\mathcal{F}_r^{\text{theory}} = \frac{\langle \psi_{\text{ideal}} | \rho_{\text{out}} | \psi_{\text{ideal}} \rangle}{\text{Tr}(|\psi_{\text{out}}\rangle\langle\psi_{\text{out}}|)}. \quad (7)$$

Here the output reduced density matrix is given by $\rho_{\text{out}} = \text{Tr}_{t,\omega}(|\psi_{\text{out}}\rangle\langle\psi_{\text{out}}|)$ which is a partial trace of the output density matrix $|\psi_{\text{out}}\rangle\langle\psi_{\text{out}}|$ over the transmitted modes and frequency states $\omega \neq \omega_1$ not detected in the reflection. The total output density matrix ρ_{out} is therefore obtained by effectively tracing out the unwanted modes. For simplicity we assume the use of perfect filters prior to detection which removes photons of frequencies other than ω_1 . The bandwidth of the etalon filters used in the experiment is ~ 3 GHz with over 95% transmission. This means the filter bandwidth is much narrower than the ground-state splitting $\Delta_h/2\pi = 7.3$ GHz but wider than the QD homogeneous linewidth $\Gamma/2\pi = 394$ MHz justifying the assumption. The fidelity in Eq. (7) is normalized by the success probability or efficiency $P_s = \text{Tr}(|\psi_{\text{out}}\rangle\langle\psi_{\text{out}}|) \equiv \sum_i \langle i |_r (|\psi_{\text{out}}\rangle\langle\psi_{\text{out}}|) |i\rangle_r$ since the protocol is conditioned on the detection of a photon in the reflection. In such case any event contributing to the loss of the scattered photon (e.g., finite cyclicity, nonzero coupling to leaky modes of the waveguide, and the transmission of a photon, which is effectively treated as loss) does not reduce the fidelity.

Using Eq. (2), the normalized output reduced density matrix is found to be

$$\frac{\rho_{\text{out}}}{P_s} = \frac{1}{2P_s} \left(|\alpha|^2 |r_1^e|^2 |e\downarrow\rangle\langle e\downarrow| - \alpha\beta^* r_1^e r_1^{l*} |e\downarrow\rangle\langle l\uparrow| - \alpha^* \beta r_1^{e*} r_1^l |l\uparrow\rangle\langle e\downarrow| + |\beta|^2 |r_1^l|^2 |l\uparrow\rangle\langle l\uparrow| + |\alpha|^2 |r_1^e|^2 |e\uparrow\rangle\langle e\uparrow| + \dots \right).$$

For instance we write out two of the matrix elements in ρ_{out} using the results from Sec. A and Eq. (6):

$$\begin{aligned} \frac{1}{2} |\alpha|^2 |r_1^e|^2 |e\downarrow\rangle\langle e\downarrow| &= \frac{1}{2} |\alpha|^2 \int_{-\infty}^{\infty} \int_{-\infty}^{\infty} d\omega d\omega' r_1(\omega) r_1^*(\omega') \Phi_1(\omega) \Phi_1(\omega') \hat{a}_e^\dagger(\omega) |\emptyset\downarrow\rangle\langle\emptyset\downarrow| \hat{a}_e(\omega'); \\ \frac{1}{2} \alpha\beta^* r_1^e r_1^{l*} |e\downarrow\rangle\langle l\uparrow| &= \frac{1}{2} \alpha\beta^* \int_{-\infty}^{\infty} \int_{-\infty}^{\infty} d\omega d\omega' r_1(\omega) r_1^*(\omega') \Phi_1(\omega) \Phi_1(\omega') \hat{a}_e^\dagger(\omega) |\emptyset\downarrow\rangle\langle\emptyset\uparrow| \hat{a}_e(\omega'), \end{aligned}$$

where $|\emptyset\rangle$ is the vacuum state. For simplicity we now say that the early and late scattering events are identical for any given input frequency thus $r_1^e = r_1^l = r_1$. The reasoning behind this is further discussed in Sec. D. Therefore, for an ideal Bell state in the reflected mode: $|\psi_{\text{ideal}}\rangle = \alpha |e\downarrow\rangle - \beta |l\uparrow\rangle$, the overlap of one of the density matrix elements

with the ideal state becomes

$$\begin{aligned}
& \langle \psi_{\text{ideal}} | \left[\frac{1}{2} |\alpha|^2 |r_1^e|^2 |e \downarrow\rangle \langle e \downarrow| \right] | \psi_{\text{ideal}} \rangle \\
&= \frac{|\alpha|^4}{2} \int_{-\infty}^{\infty} \int_{-\infty}^{\infty} \int_{-\infty}^{\infty} d\omega d\omega' d\omega'' \langle \emptyset \downarrow | \hat{a}_e(\omega'') \left[r_1(\omega) r_1^*(\omega') \Phi_1(\omega) \Phi_1(\omega') \hat{a}_e^\dagger(\omega) | \emptyset \downarrow \rangle \langle \emptyset \downarrow | \hat{a}_e(\omega') \right] \hat{a}_e^\dagger(\omega'') | \emptyset \downarrow \rangle \\
&= \frac{|\alpha|^4}{2} \int_{-\infty}^{\infty} \int_{-\infty}^{\infty} \int_{-\infty}^{\infty} d\omega d\omega' d\omega'' r_1(\omega) r_1^*(\omega') \Phi_1(\omega) \Phi_1(\omega') \delta(\omega - \omega'') \delta(\omega' - \omega'') \\
&= \frac{|\alpha|^4}{2} \int_{-\infty}^{\infty} |\Phi_1(\omega)|^2 |r_1(\omega)|^2 d\omega.
\end{aligned}$$

Including all terms, the conditional fidelity is found to be

$$\mathcal{F}_r^{\text{theory}} = \frac{1}{2P_s} \int_{-\infty}^{\infty} |\Phi_1(\omega)|^2 |r_1(\omega)|^2 d\omega, \quad (8)$$

where the success probability P_s is the trace of the output density matrix over the four basis states $|i\rangle = \{|e \uparrow\rangle_r, |e \downarrow\rangle_r, |l \uparrow\rangle_r, |l \downarrow\rangle_r\}$ in the Hilbert space of the spin-photon system. It is given by

$$P_s = \text{Tr}(|\psi_{\text{out}}\rangle \langle \psi_{\text{out}}|) = \sum_i \langle i|_r (|\psi_{\text{out}}\rangle \langle \psi_{\text{out}}|) |i\rangle_r = \frac{1}{2} \left[\int_{-\infty}^{\infty} |\Phi_1(\omega)|^2 |r_1(\omega)|^2 d\omega + \int_{-\infty}^{\infty} |\Phi_1(\omega)|^2 |\hat{r}_1(\omega)|^2 d\omega \right]. \quad (9)$$

Combining Eqs. (8) and (9) results in the formula for the entanglement fidelity conditioned on reflected photons

$$\boxed{\mathcal{F}_r^{\text{theory}} = \frac{\int_{-\infty}^{\infty} |\Phi_1(\omega)|^2 |r_1(\omega)|^2 d\omega}{\int_{-\infty}^{\infty} |\Phi_1(\omega)|^2 |r_1(\omega)|^2 d\omega + \int_{-\infty}^{\infty} |\Phi_1(\omega)|^2 |\hat{r}_1(\omega)|^2 d\omega}}. \quad (10)$$

D. Perturbative Form of the Entanglement Fidelity

The two integrals in Eq. (10) are the probabilities of scattering a photon of frequency ω_1 from the spin state $|\uparrow\rangle$ (resonant) and from $|\downarrow\rangle$ (off-resonant) respectively. In particular, using Eq. (4) we find

$$\begin{aligned}
\int_{-\infty}^{\infty} |\Phi_1(\omega)|^2 |r_1(\omega)|^2 d\omega &= \frac{1}{\sqrt{2\pi\sigma_o^2}} \int_{-\infty}^{\infty} e^{-\frac{(\omega-\omega_1)^2}{2\sigma_o^2}} \left| -\frac{2\sqrt{\Gamma_1^t \Gamma_1^r}}{\Gamma + 2i\delta_1} \right|^2 d\omega \approx 1 - \frac{4\sigma_o^2}{\Gamma^2} - \frac{\Gamma^2 - \Gamma_1^2}{\Gamma^2}; \\
\int_{-\infty}^{\infty} |\Phi_1(\omega)|^2 |\hat{r}_1(\omega)|^2 d\omega &\approx \frac{\Gamma_1^2}{\Gamma^2 + 4\Delta_h^2},
\end{aligned} \quad (11)$$

where we assume that the scattered photon is equally coupled to the reflected and transmitted modes, i.e., $\Gamma_i^r = \Gamma_i^t = \Gamma_i/2$. σ_o is the standard deviation of the spectral width of the incident Gaussian pulse. In evaluating Eq. (11) perturbatively we assume the frequency detuning δ_1 to be small compared to the QD total decay rate Γ and the ground-state splitting Δ_h for efficient light-matter interaction.

1. Spectral mode mismatch

Conditioning on the detection of a reflected photon of frequency ω_1 within the time-bin window, the entanglement fidelity becomes immune to the spectral error due to the nonzero bandwidth σ_o of the incident pulse to lowest order in perturbation theory. Using Eqs. (10) and (11), the resultant fidelity is

$$\mathcal{F}_r^{\text{theory}} \approx 1. \quad (12)$$

Simply stated, photons which are not resonant with the QD transition will be transmitted instead of reflected. Since the protocol is conditioned on the reflection of either an early or a late photon, the transmission of the photon only reduces the success probability. The fidelity thus approaches unity as long as the dynamics of the early and late

scattering events are identical. The same argument can be made for the broadening of the QD optical transition due to slow spectral wandering. Due to the ms-long spectral diffusion time [5], the QD resonance drift is constant over its lifetime (0.4 ns) and also the interferometric delay (11.8 ns), the QD reflectivity is thus identical for both early and late scattering events without impacts on the entanglement fidelity. The spectral jittering on the QD resonance is modelled by taking $\delta_1 = \omega_1 - \omega \rightarrow \delta_1 + \delta_e$ where δ_e follows a Gaussian spectral diffusion profile $N(0, \sigma_e)$ [2].

If the protocol is post-selected on the presence of transmitted photon; however, the fidelity becomes susceptible to the spectral mismatch error. A similar analysis shows

$$\mathcal{F}_t^{\text{theory}} \approx 1 - \frac{4\sigma_o^2}{\Gamma^2} - \frac{4\sigma_e^2}{\Gamma^2}, \quad (13)$$

as the spectral infidelity arises from incomplete destructive interference between the incident field and the resonantly scattered photon ($t_1 \neq 0$). Any spectral effects reducing this interference would stain the quality of the entangled state. It is important to note that despite the QD spectral reflectivity, there is still a small probability of detecting undesired Raman photons of frequency $\omega_2 = \omega_1 + \Delta_h$ in the reflection due to the finite optical cyclicity. These photons result from the imperfect QD two-level system and are filtered out.

2. Finite cyclicity and coupling loss

On the reflection port, photons could either originate from **(i)** resonant reflection on the spin-preserving transition (indicated by r_1), **(ii)** resonant Raman spin-flip process to $|\downarrow\rangle$ (r_2), or **(iii)** off-resonant reflection from $|\downarrow\rangle$ (\hat{r}_1). A high cyclicity reduces the probability of resonant spin-flip process but strengthens off-resonant reflection. The undesired events (ii) and (iii) can be reduced by having a larger ground-state splitting $\Delta_h \gg \Gamma$. Additionally, coupling to lossy modes of the waveguide implies that the reflected photons are lost without being detected; as a result these events do not affect the fidelity. Effectively we find

$$\mathcal{F}_r^{\text{theory}} \approx 1 - \frac{\Gamma^2}{4\Delta_h^2} \left(\frac{C}{C+1} \beta \right)^2. \quad (14)$$

We observe that the fidelity is indeed robust to coupling loss and optical cyclicity, and is mainly reduced due to finite probability $\sim \Gamma^2/\Delta_h^2$ of detecting Rayleigh-scattered photons from $|\downarrow\rangle$. Note that when deriving Eq. (14) we define the optical cyclicity $C \equiv \Gamma_1/\Gamma_2$ [6], the total decay rate $\Gamma = \Gamma_1 + \Gamma_2 + \gamma_1 + \gamma_2$ where γ_1 (γ_2) is the radiative rate from the transition $|e\rangle \rightarrow |\uparrow\rangle$ ($|e\rangle \rightarrow |\downarrow\rangle$) which couples to lossy modes. The waveguide-coupling efficiency $\beta \equiv (\Gamma_1 + \Gamma_2)/\Gamma$. From these conditions we obtain $\Gamma_1 = \frac{C}{C+1} \beta \Gamma$ which is then substituted into Eq. (11).

3. Phonon-induced pure dephasing

The interaction of the QD with a phononic environment results in the broadening of the zero-phonon line and a broad phonon sideband [7–10]. The latter can be filtered out while the former contributes to the reflection of incoherent photons which scramble the phase coherence of the spin-photon Bell state. The incoherent photons are only slightly broadened and thus cannot easily be removed by filters.

We follow the approach in Ref. [2] and model this incoherent process as Markovian decoherence given by a dephasing rate γ_d with the Lindblad operator $\sqrt{2\gamma_d} \hat{\sigma}_{ee}$ where $|e\rangle_s \equiv |\uparrow\downarrow\rangle$ is the atomic excited state. The dephasing leads to a quantum jump to the excited state (with a dephasing probability P_{γ_d}) followed by the decay to either of the two hole ground states with probabilities set by the transition rates Γ_i/Γ . The emitted photon into the waveguide is represented by a normalized photon density matrix $\rho_{\gamma_d}^{\omega_i}$. This is described by the density matrix

$$\rho' = \rho + P_{\gamma_d}^{\omega_1} \rho_{\gamma_d}^{\omega_1} \otimes |\uparrow\rangle \langle \uparrow|, \quad (15)$$

where ρ is the density matrix without a dephasing quantum jump. Initially there are also incoherent photons of frequency ω_2 due to finite optical cyclicity but these are subsequently filtered out together with phonon sidebands. $\rho_{\gamma_d}^{\omega_1} \otimes |\uparrow\rangle \langle \uparrow|$ is the photon density matrix resulting from the incoherent dephasing with a probability $P_{\gamma_d}^{\omega_1}$ given by

$$P_{\gamma_d}^{\omega_1} = \frac{\Gamma_1^r}{\Gamma} P_{\gamma_d} = \frac{\Gamma_1^r}{\Gamma} \int_{-\infty}^{\infty} e^{-\frac{(\omega-\omega_1)^2}{2\sigma_o^2}} \left| \frac{-2\sqrt{2\gamma_d}\Gamma_1^r}{\Gamma + 2i(\omega - \omega_1)} \right|^2 d\omega = \frac{2\gamma_d}{\Gamma} \int_{-\infty}^{\infty} |\Phi_1(\omega)|^2 |r_1(\omega)|^2 d\omega. \quad (16)$$

where $\Gamma_1^r = \Gamma_1/2$ is the decay rate in the reflected mode.

To evaluate the effect of pure dephasing in the entanglement protocol, it is instructive to consider the propagation of the error as there are two separate scattering events which will both lead to incoherent decay. Since Eq. (15) depends on whether there is a quantum jump to the excited state, we can assume that pure dephasing occurs primarily when the incident photon is resonant with the QD state since the excited state is unlikely to be populated via off-resonant scattering. As such, using Eq. (15) there are two additional incoherent density matrices in the normalized output reduced density matrix

$$\rho'_{\text{out}} = \frac{P_s \rho_{\text{out}} + \frac{1}{2} |\alpha|^2 P_{\gamma_d}^{\omega_1} \rho_{\gamma_d}^{\omega_1, e} \otimes \hat{R}_y(\pi) |\uparrow\rangle \langle \uparrow| \hat{R}_y^\dagger(\pi) + \frac{1}{2} |\beta|^2 P_{\gamma_d}^{\omega_1} \rho_{\gamma_d}^{\omega_1, l} \otimes |\uparrow\rangle \langle \uparrow|}{P_s + \text{Tr}\left(\frac{1}{2} |\alpha|^2 P_{\gamma_d}^{\omega_1} \rho_{\gamma_d}^{\omega_1, e} \otimes \hat{R}_y(\pi) |\uparrow\rangle \langle \uparrow| \hat{R}_y^\dagger(\pi)\right) + \text{Tr}\left(\frac{1}{2} |\beta|^2 P_{\gamma_d}^{\omega_1} \rho_{\gamma_d}^{\omega_1, l} \otimes |\uparrow\rangle \langle \uparrow|\right)}. \quad (17)$$

Using Eq. (16) with $|\alpha| = |\beta| = 1/\sqrt{2}$, the entanglement fidelity under pure dephasing is

$$\mathcal{F}_r^{\text{theory}} = \langle \psi_{\text{ideal}} | \rho'_{\text{out}} | \psi_{\text{ideal}} \rangle = \frac{\int_{-\infty}^{\infty} |\Phi_1(\omega)|^2 |r_1(\omega)|^2 d\omega + (|\alpha|^4 + |\beta|^4) P_{\gamma_d}^{\omega_1}}{\int_{-\infty}^{\infty} |\Phi_1(\omega)|^2 |r_1(\omega)|^2 d\omega + \int_{-\infty}^{\infty} |\Phi_1(\omega)|^2 |\hat{r}_1(\omega)|^2 d\omega + P_{\gamma_d}^{\omega_1}} \approx 1 - \frac{\gamma_d}{\Gamma}. \quad (18)$$

4. Spin dephasing

In this section, we investigate how the decoherence of the spin states affects the entanglement fidelity. Specifically we consider the dephasing of the QD spin ground states, due to the presence of an external Overhauser field effectively formed by a neighboring nuclear ensemble [11]. This effect causes a superposition spin qubit to precess on the equatorial plane at a random frequency δ_g slower than the QD decay rate, which can be modelled by applying a time-evolution operator $\hat{T}(\Delta t) = \exp(-i\delta_g \hat{S}_z \Delta t)$ on the superposition spin state, where $\hat{S}_z = \hat{\sigma}_z/2$ [2]. During the entanglement sequence, a π -pulse is applied between two scattering events to ensure the precession of the spin is reversed and thus the spin is eventually refocused. In theory, the superposition qubit starts to precess at t_0 and the π -rotation pulse is applied at t_π . The spin is then refocused and read out at t_r where $t_r - t_\pi = t_\pi - t_0 = \Delta t$ must be satisfied for the perfect echo condition. For this model, the Overhauser field is assumed to be dominated by low-frequency nuclear noise $\omega \ll \frac{1}{2\Delta t}$ thus it is treated as quasi-static (“frozen” [12]) over the course of the experiment. The quantity of interest as a function of small drift δ_g can then be averaged with the Gaussian distribution $N(\delta_g, \sigma_{\text{OH}})$ where σ_{OH} is the standard deviation in Overhauser field fluctuations.

To understand how spin echo benefits the entanglement protocol, we introduce the spin-echo operator $\hat{U}_{\text{echo}} \equiv \hat{T}(t_r - t_\pi) \hat{R}_y(\pi) \hat{T}(t_\pi - t_0)$ which transforms the spin states into

$$\begin{cases} \hat{U}_{\text{echo}} |\uparrow\rangle = -\exp\left(\frac{-i\delta_g(2t_\pi - t_r - t_0)}{2}\right) |\downarrow\rangle \equiv \lambda_\downarrow |\downarrow\rangle; \\ \hat{U}_{\text{echo}} |\downarrow\rangle = \exp\left(\frac{i\delta_g(2t_\pi - t_r - t_0)}{2}\right) |\uparrow\rangle \equiv \lambda_\uparrow |\uparrow\rangle. \end{cases} \quad (19)$$

With Eq. (19), the normalized output state in Eq. (2) becomes

$$|\psi_{\text{out}}\rangle = -\alpha \lambda_\downarrow r_1^e |e \downarrow\rangle_r + \alpha \lambda_\uparrow r_1^e |e \uparrow\rangle_r + \beta \lambda_\uparrow r_1^l |l \uparrow\rangle_r - \beta \lambda_\downarrow r_1^l |l \downarrow\rangle_r + \dots \quad (20)$$

Eq. (20) implies that the phase coherence between $|e \downarrow\rangle_r$ and $|l \uparrow\rangle_r$ depends on **(i)** the accumulated phase from spin precession, and **(ii)** the phase acquired from the early and late single-photon scattering events which is determined by the *exact time* of scattering occurred within the optical pulse. Condition **(ii)** is made equal by interfering the time-bins with a matching time delay $\tau = 11.8$ ns on the detection path. Since the time-bin qubit is created and measured using the same interferometer setup, by having an equal time delay $\tau_e = \tau_d = \tau$ for the excitation and detection paths, the interferometer temporally picks out events in which the exact time of scattering is in the same position of the pulse, i.e., $r_1^e(t') = r_1^l(t')$ for some time $t' \in \Phi_1(t)$ within the optical pulse.

Now, to study how condition **(i)** affects the entanglement fidelity, we assume perfect single-photon scattering and consider only the output state conditioned on reflected photons, thus Eq. (20) is simplified as

$$|\psi_{\text{out}}\rangle = \alpha \lambda_\downarrow |e \downarrow\rangle_r - \beta \lambda_\uparrow |l \uparrow\rangle_r. \quad (21)$$

For measuring the output state in the Z-basis, we compute the expectation value of the Z-basis projection operator $\hat{P}_z \equiv |e \downarrow\rangle_r \langle e \downarrow|_r + |l \uparrow\rangle_r \langle l \uparrow|_r$ [13, 14]

$$\langle \hat{P}_z \rangle \equiv \langle \psi_{\text{out}} | \hat{P}_z | \psi_{\text{out}} \rangle = |\alpha \lambda_\downarrow|^2 + |\beta \lambda_\uparrow|^2 = 1, \quad (22)$$

which is insensitive to spin dephasing, regardless of whether the echo condition is fulfilled. However, when measuring in the X- (Y-basis), the corresponding expectation value of \hat{M}_x (\hat{M}_y) averaged over $N(\delta_g, \sigma_{\text{OH}})$ is

$$\begin{aligned}\langle \hat{M}_x \rangle &= \int_{-\infty}^{\infty} \langle \psi_{\text{out}}^x | \hat{M}_x | \psi_{\text{out}}^x \rangle N(\delta_g, \sigma_{\text{OH}}) d\delta_g = - \int_{-\infty}^{\infty} \cos \frac{\delta_g \Delta \tau}{2} N(\delta_g, \sigma_{\text{OH}}) d\delta_g = -e^{-(\Delta \tau / T_2^*)^2}; \\ \langle \hat{M}_y \rangle &= \int_{-\infty}^{\infty} \langle \psi_{\text{out}}^y | \hat{M}_y | \psi_{\text{out}}^y \rangle N(\delta_g, \sigma_{\text{OH}}) d\delta_g = e^{-(\Delta \tau / T_2^*)^2},\end{aligned}\quad (23)$$

with the output state (Eq. (21)) rewritten in the X- (Y-basis)

$$\begin{aligned}|\psi_{\text{out}}^x\rangle &= \frac{1}{2} [(\lambda_{\downarrow} - \lambda_{\uparrow}) |X_p^+ X_s^+\rangle - (\lambda_{\uparrow} + \lambda_{\downarrow}) |X_p^+ X_s^-\rangle + (\lambda_{\uparrow} + \lambda_{\downarrow}) |X_p^- X_s^+\rangle + (\lambda_{\uparrow} - \lambda_{\downarrow}) |X_p^- X_s^-\rangle]; \\ |\psi_{\text{out}}^y\rangle &= \frac{1}{2} [-i(\lambda_{\uparrow} + \lambda_{\downarrow}) |Y_p^+ Y_s^+\rangle + i(\lambda_{\uparrow} - \lambda_{\downarrow}) |Y_p^+ Y_s^-\rangle + (\lambda_{\downarrow} - \lambda_{\uparrow}) |Y_p^- Y_s^+\rangle + (\lambda_{\downarrow} + \lambda_{\uparrow}) |Y_p^- Y_s^-\rangle],\end{aligned}\quad (24)$$

and the respective projection operators

$$\begin{aligned}\hat{M}_x &= |X_p^+ X_s^+\rangle \langle X_p^+ X_s^+| + |X_p^- X_s^-\rangle \langle X_p^- X_s^-| - |X_p^+ X_s^-\rangle \langle X_p^+ X_s^-| - |X_p^- X_s^+\rangle \langle X_p^- X_s^+|; \\ \hat{M}_y &= |Y_p^+ Y_s^+\rangle \langle Y_p^+ Y_s^+| + |Y_p^- Y_s^-\rangle \langle Y_p^- Y_s^-| - |Y_p^+ Y_s^-\rangle \langle Y_p^+ Y_s^-| - |Y_p^- Y_s^+\rangle \langle Y_p^- Y_s^+|.\end{aligned}\quad (25)$$

Eq. (23) shows a Gaussian decay with spin dephasing time $T_2^* = \sqrt{2}/\sigma_{\text{OH}}$ when the echo condition $\Delta \tau \equiv 2t_{\pi} - t_r - t_0 \neq 0$ is not met. For that reason, to measure spin-photon correlations in the equatorial bases, a second $\hat{R}_y(\pi/2)$ pulse is applied at $t_r = 2t_{\pi} - t_0$ to rotate the spin state to either of its two poles to prevent subsequent precession. From here, we note that for Z-basis fidelity measurements, the second $\hat{R}_y(\pi/2)$ pulse is not necessary as $\langle \hat{P}_z \rangle$ is tolerant to spin dephasing error. In such a case, the central π -rotation pulse does not play a refocusing role but is still required for inverting the spin between two scattering events. Additionally, due to having identical rotational pulse sequence, the spin-echo visibility V_s measured in Figure 2d of the main text in principle establishes an upper bound for $|\langle \hat{M}_x \rangle|$ and $|\langle \hat{M}_y \rangle|$, while $\langle \hat{P}_z \rangle$ is primarily limited by fidelity of the $\hat{R}_y(\pi)$ pulse.

Note that Eq. (24) is derived from Eq. (21) taking $\beta = \alpha e^{i\theta_0} = \alpha$ for $|\psi_{\text{out}}^x\rangle$ ($\beta = \alpha e^{i(\theta_0 + \pi/2)} = i\alpha$ for $|\psi_{\text{out}}^y\rangle$) (see Methods), where $|e\rangle \equiv |X_p^+\rangle + |X_p^-\rangle = |Y_p^+\rangle + |Y_p^-\rangle$ and $|l\rangle \equiv |X_p^+\rangle - |X_p^-\rangle = |Y_p^+\rangle - |Y_p^-\rangle$. The ideal case of Eq. (24) can be shown to be consistent with the experimental spin-photon correlations in Figures 3c-d (main text) taking $\Delta \tau = 0$.

5. Incoherent spin-flip error and finite T_2^*

The next error concerns spin decoherence induced by the red-detuned spin rotation laser and due to finite spin coherence time T_2^* . The former effect has been observed in Refs. [13, 15] which results in power-dependent spin-flips, thereby destroying the coherence of the spin qubit during spin rotations. Despite its exact origin not being fully resolved, its effect on the spin coherence and the fidelity can be approximated by modelling the spin-flip error by a depolarizing channel $\mathcal{E}_{\text{depol}}^s$, with the probability of undergoing a random spin-flip p dependent on the incoherent spin-flip rate κ and the duration of the respective rotation pulse T_r . The action of the depolarizing channel on a density matrix ρ is denoted by $\mathcal{E}_{\text{depol}}(\rho) = (1-p)\rho + p\mathcal{I}/2$, where \mathcal{I} is the identity matrix. As an example, after applying a $\hat{R}_y(\pi/2)$ pulse on a spin state initialized in $|\downarrow\rangle$, the spin density matrix transforms according to

$$\begin{aligned}\mathcal{E}_{\text{depol}}^s \left(\hat{R}_y^i(\pi/2) \rho_{\downarrow} \hat{R}_y^{i\dagger}(\pi/2) \right) &= \mathcal{E}_{\text{depol}}^s \left(\mathcal{F}_{\frac{\pi}{2}} \hat{R}_y(\pi/2) \rho_{\downarrow} \hat{R}_y^\dagger(\pi/2) + (1 - \mathcal{F}_{\frac{\pi}{2}}) \rho_{-} \right) \\ &= (1 - p_{\pi/2}) \left(\mathcal{F}_{\frac{\pi}{2}} \hat{R}_y(\pi/2) \rho_{\downarrow} \hat{R}_y^\dagger(\pi/2) + (1 - \mathcal{F}_{\frac{\pi}{2}}) \rho_{-} \right) + \frac{p_{\pi/2}}{2} \mathcal{I} \\ &= \begin{bmatrix} \frac{1}{2} & (1 - p_{\pi/2})(\mathcal{F}_{\frac{\pi}{2}} - \frac{1}{2}) \\ (1 - p_{\pi/2})(\mathcal{F}_{\frac{\pi}{2}} - \frac{1}{2}) & \frac{1}{2} \end{bmatrix} \equiv \mathbf{E}_{\pi/2},\end{aligned}\quad (26)$$

where ρ_{\downarrow} is the initial spin density matrix and $\rho_{-} \equiv |-\rangle_s \langle -|_s$. $\mathbf{E}_{\pi/2}$ is the output density matrix. In addition to the incoherent spin flip with a probability $p_{\pi/2}$ we here include known imperfections of the rotation pulse $\hat{R}_y^i(\pi/2)$, which has a fidelity of $\mathcal{F}_{\frac{\pi}{2}}$ to coherently rotate the spin to the superposition state $|+\rangle_s$ and a probability of $1 - \mathcal{F}_{\frac{\pi}{2}}$ to project onto $|-\rangle_s$. The fidelity of *coherent* $\pi/2$ -spin rotation is determined by limitations of the two-photon Raman

scheme, which is dominated by finite spin coherence time T_2^* and the power-dependent rate γ_r (Supplementary Note 6):

$$\mathcal{F}_{\pi/2} \approx (1 - \gamma_r T_{\pi/2}) \times \mathcal{F}_{\pi/2}(T_2^*), \quad (27)$$

where the $\pi/2$ -rotation fidelity under the Overhauser field noise $\sigma_{\text{OH}} = \sqrt{2}/T_2^*$ is expressed by

$$\mathcal{F}_{\pi/2}(T_2^*) \equiv \left| \langle \downarrow | \hat{U}_{rot,ideal}^\dagger \hat{U}_{rot} | \downarrow \rangle \right|^2 = \int_{-\infty}^{\infty} \frac{\Delta_{\text{OH}}^2 + \Omega_r(\Omega_r + \sqrt{\Omega_r^2 + \Delta_{\text{OH}}^2})}{2(\Omega_r^2 + \Delta_{\text{OH}}^2)} N(0, \sigma_{\text{OH}}) d\delta_g \approx 1 - \frac{2}{\pi^2} \left(\frac{T_{\pi/2}}{T_2^*} \right)^2, \quad (28)$$

for a pulse duration of $T_{\pi/2}$. Eq. (28) is derived following the notations in Ref. [16] where $\theta \equiv \frac{T_{\pi/2}}{2} \sqrt{\Omega_r^2 + \Delta_{\text{OH}}^2} = \pi/4$, and Ω_r is the spin-rotation Rabi frequency with $\Omega_r T_{\pi/2} = \pi/2$. \mathcal{F}_π can also be derived similarly. The probability of introducing a depolarizing error $p_{\pi/2}$ during a $\hat{R}_y(\pi/2)$ rotation is estimated by integrating the exponential distribution over the pulse duration for a given incoherent spin-flip rate κ :

$$p_{\pi/2} = \int_0^{T_{\pi/2}} \kappa e^{-\kappa t} dt = 1 - e^{-\kappa T_{\pi/2}}. \quad (29)$$

The exponential distribution describes the probability of a random spin-flip occurring in a certain time period, where the spin-flip event is assumed not to depend on how much time has passed in the protocol (i.e. it is memory-less). Similarly, for a $\hat{R}_y(\pi)$ pulse applied on an arbitrary spin state ρ_s ,

$$\begin{aligned} \mathcal{E}_{\text{depol}}^s \left(\hat{R}_y^i(\pi) \rho_s \hat{R}_y^{i\dagger}(\pi) \right) &= (1 - p_\pi) \left(\mathcal{F}_\pi \hat{R}_y(\pi) \rho_s \hat{R}_y^\dagger(\pi) + (1 - \mathcal{F}_\pi) \rho_s \right) + \frac{p_\pi}{2} \mathcal{I} \\ &= \begin{bmatrix} (1 - p_\pi)[\mathcal{F}_\pi \rho_4 + (1 - \mathcal{F}_\pi) \rho_1] + \frac{p_\pi}{2} & (1 - p_\pi)[-\mathcal{F}_\pi \rho_3 + (1 - \mathcal{F}_\pi) \rho_2] \\ (1 - p_\pi)[-\mathcal{F}_\pi \rho_2 + (1 - \mathcal{F}_\pi) \rho_3] & (1 - p_\pi)[\mathcal{F}_\pi \rho_1 + (1 - \mathcal{F}_\pi) \rho_4] + \frac{p_\pi}{2} \end{bmatrix} \equiv \mathbf{E}_\pi, \end{aligned} \quad (30)$$

where the initial spin density matrix is

$$\rho_s \equiv \begin{bmatrix} \rho_1 & \rho_2 \\ \rho_3 & \rho_4 \end{bmatrix}, \quad (31)$$

and p_π is the probability of introducing the depolarizing error during a $\hat{R}_y(\pi)$ rotation found similarly as in Eq. (29). As a quick sanity check, using Eq. (30) and $\rho_1 = \rho_2 = \rho_3 = 0$, $\rho_4 = 1$, the total π -rotation pulse fidelity which includes the contribution from both coherent and incoherent spin-flip processes can be estimated to be

$$\mathcal{F}_{\pi,\text{total}} = (1 - p_\pi) \mathcal{F}_\pi + \frac{p_\pi}{2} = (1 - p_\pi) \times (1 - \gamma_r T_\pi) \times \mathcal{F}_\pi(T_2^*) + \frac{p_\pi}{2} \approx 1 - \frac{1}{2}(\kappa + 2\gamma_r) T_\pi - \frac{2}{\pi^2} \left(\frac{T_\pi}{T_2^*} \right)^2. \quad (32)$$

Using experimental values for the incoherent spin-flip rate $\kappa = 0.0098 \text{ ns}^{-1}$ and $\gamma_r = 0.0081 \text{ ns}^{-1}$ extracted in Supplementary Note 6 with spin dephasing time $T_2^* = 23.2 \text{ ns}$ [13], we estimate $\mathcal{F}_{\pi,\text{total}} \approx 89.8\%$ for $T_\pi = 7 \text{ ns}$, which indeed agrees with the measured value of $F_\pi = (88.1 \pm 3.8)\%$ (Supplementary Note 6).

Now we consider the evolution of the spin-photon system during the entanglement protocol. The protocol begins by preparing a time-bin photonic qubit ρ_p and a spin state in ρ_s :

$$\begin{aligned}
\rho_p \otimes \rho_s &= \begin{bmatrix} |\alpha|^2 & \alpha^* \beta \\ \alpha \beta^* & |\beta|^2 \end{bmatrix} \otimes \begin{bmatrix} 0 & 0 \\ 0 & 1 \end{bmatrix} \\
\begin{matrix} \hat{R}_y(\pi/2) \\ \hat{S}_e \\ \hat{R}_y(\pi) \\ \hat{S}_l \end{matrix} \longrightarrow & (\mathcal{I} \otimes \mathcal{E}_{\text{depol}}^s)(\rho_p \otimes \rho_s) = \begin{bmatrix} |\alpha|^2 \mathbf{E}_{\pi/2} & \alpha^* \beta \mathbf{E}_{\pi/2} \\ \alpha \beta^* \mathbf{E}_{\pi/2} & |\beta|^2 \mathbf{E}_{\pi/2} \end{bmatrix} \equiv \begin{bmatrix} |\alpha|^2 \begin{bmatrix} E_{\pi/2}^1 & E_{\pi/2}^2 \\ E_{\pi/2}^3 & E_{\pi/2}^4 \end{bmatrix} & \alpha^* \beta \begin{bmatrix} E_{\pi/2}^1 & E_{\pi/2}^2 \\ E_{\pi/2}^3 & E_{\pi/2}^4 \end{bmatrix} \\ \alpha \beta^* \begin{bmatrix} E_{\pi/2}^1 & E_{\pi/2}^2 \\ E_{\pi/2}^3 & E_{\pi/2}^4 \end{bmatrix} & |\beta|^2 \begin{bmatrix} E_{\pi/2}^1 & E_{\pi/2}^2 \\ E_{\pi/2}^3 & E_{\pi/2}^4 \end{bmatrix} \end{bmatrix} \\
& \begin{bmatrix} |\alpha|^2 \begin{bmatrix} |r_1^e|^2 E_{\pi/2}^1 & r_1^{e*} \hat{r}_1^e E_{\pi/2}^2 \\ r_1^e \hat{r}_1^{e*} E_{\pi/2}^3 & |\hat{r}_1^e|^2 E_{\pi/2}^4 \end{bmatrix} & \alpha^* \beta \begin{bmatrix} r_1^{e*} E_{\pi/2}^1 & r_1^{e*} E_{\pi/2}^2 \\ \hat{r}_1^{e*} E_{\pi/2}^3 & \hat{r}_1^{e*} E_{\pi/2}^4 \end{bmatrix} \\ \alpha \beta^* \begin{bmatrix} r_1^e E_{\pi/2}^1 & \hat{r}_1^e E_{\pi/2}^2 \\ r_1^e E_{\pi/2}^3 & \hat{r}_1^e E_{\pi/2}^4 \end{bmatrix} & |\beta|^2 \begin{bmatrix} E_{\pi/2}^1 & E_{\pi/2}^2 \\ E_{\pi/2}^3 & E_{\pi/2}^4 \end{bmatrix} \end{bmatrix} \equiv \begin{bmatrix} |\alpha|^2 \begin{bmatrix} \rho_1^1 & \rho_1^2 \\ \rho_1^3 & \rho_1^4 \end{bmatrix} & \alpha^* \beta \begin{bmatrix} \rho_2^1 & \rho_2^2 \\ \rho_2^3 & \rho_2^4 \end{bmatrix} \\ \alpha \beta^* \begin{bmatrix} \rho_3^1 & \rho_3^2 \\ \rho_3^3 & \rho_3^4 \end{bmatrix} & |\beta|^2 \begin{bmatrix} \rho_4^1 & \rho_4^2 \\ \rho_4^3 & \rho_4^4 \end{bmatrix} \end{bmatrix} \\
& \begin{bmatrix} |\alpha|^2 \begin{bmatrix} E_{\pi}^1(\rho_1^4, \rho_1^1) & E_{\pi}^2(\rho_1^3, \rho_1^2) \\ E_{\pi}^3(\rho_2^2, \rho_2^3) & E_{\pi}^4(\rho_1^1, \rho_1^4) \end{bmatrix} & \alpha^* \beta \begin{bmatrix} E_{\pi}^1(\rho_2^4, \rho_2^1) & E_{\pi}^2(\rho_2^3, \rho_2^2) \\ E_{\pi}^3(\rho_2^2, \rho_2^3) & E_{\pi}^4(\rho_1^1, \rho_1^4) \end{bmatrix} \\ \alpha \beta^* \begin{bmatrix} E_{\pi}^1(\rho_3^4, \rho_3^1) & E_{\pi}^2(\rho_3^3, \rho_3^2) \\ E_{\pi}^3(\rho_2^2, \rho_2^3) & E_{\pi}^4(\rho_1^1, \rho_1^4) \end{bmatrix} & |\beta|^2 \begin{bmatrix} E_{\pi}^1(\rho_4^4, \rho_4^1) & E_{\pi}^2(\rho_3^3, \rho_3^2) \\ E_{\pi}^3(\rho_2^2, \rho_2^3) & E_{\pi}^4(\rho_1^1, \rho_1^4) \end{bmatrix} \end{bmatrix} \\
& \begin{bmatrix} |\alpha|^2 \begin{bmatrix} E_{\pi}^1(\rho_1^4, \rho_1^1) & E_{\pi}^2(\rho_1^3, \rho_1^2) \\ E_{\pi}^3(\rho_2^2, \rho_2^3) & E_{\pi}^4(\rho_1^1, \rho_1^4) \end{bmatrix} & \alpha^* \beta \begin{bmatrix} r_1^l E_{\pi}^1(\rho_2^4, \rho_2^1) & \hat{r}_1^l E_{\pi}^2(\rho_2^3, \rho_2^2) \\ r_1^l E_{\pi}^3(\rho_2^2, \rho_2^3) & \hat{r}_1^l E_{\pi}^4(\rho_1^1, \rho_1^4) \end{bmatrix} \\ \alpha \beta^* \begin{bmatrix} r_1^{l*} E_{\pi}^1(\rho_3^4, \rho_3^1) & \boxed{r_1^{l*} E_{\pi}^2(\rho_3^3, \rho_3^2)} \\ \hat{r}_1^{l*} E_{\pi}^3(\rho_2^2, \rho_2^3) & \boxed{\hat{r}_1^{l*} E_{\pi}^4(\rho_1^1, \rho_1^4)} \end{bmatrix} & |\beta|^2 \begin{bmatrix} |r_1^l|^2 E_{\pi}^1(\rho_4^4, \rho_4^1) & \hat{r}_1^l r_1^{l*} E_{\pi}^2(\rho_3^3, \rho_3^2) \\ \hat{r}_1^{l*} r_1^l E_{\pi}^3(\rho_2^2, \rho_2^3) & \boxed{|\hat{r}_1^l|^2 E_{\pi}^4(\rho_1^1, \rho_1^4)} \end{bmatrix} \end{bmatrix} \equiv \rho_{\text{out}}. \quad (33)
\end{aligned}$$

Here the basis states spanning $\rho_p \otimes \rho_s$ are $\{|e \uparrow\rangle_r, |e \downarrow\rangle_r, |l \uparrow\rangle_r, |l \downarrow\rangle_r\}$ which govern only the Hilbert space formed by the reflected photon and spin, as events in which photons are transmitted do not contribute to the fidelity. Note that when applying the $\hat{R}_y(\pi)$ pulse, we apply Eq. (30) to each of the four 2×2 blocks (which consists of spin density matrix elements ρ_j^i). For instance, the inner product $|e \downarrow\rangle_r \langle e \uparrow|_r$ has a matrix element $E_{\pi}^3(\rho_1^3, \rho_1^2)$, which corresponds to the (1,2)-th entry of the matrix \mathbf{E}_{π} with $\rho_3 \rightarrow \rho_1^3$ and $\rho_2 \rightarrow \rho_1^2$. Only the boxed terms of Eq. (33) contribute to the fidelity. As an example we evaluate one of the matrix elements $|e \uparrow\rangle_r \langle e \uparrow|_r$:

$$|\alpha|^2 E_{\pi}^1(\rho_1^4, \rho_1^1) = |\alpha|^2 \left[(1 - p_{\pi})[\mathcal{F}_{\pi} \rho_1^4 + (1 - \mathcal{F}_{\pi}) \rho_1^1] + \frac{p_{\pi}}{2} \right] = |\alpha|^2 \left[\frac{(1 - p_{\pi})}{2} [\mathcal{F}_{\pi} |\hat{r}_1^e|^2 + (1 - \mathcal{F}_{\pi}) |r_1^e|^2] + \frac{p_{\pi}}{2} \right]. \quad (34)$$

For an ideal state of $|\psi_{\text{ideal}}\rangle = (\alpha |e \downarrow\rangle_r - \beta |l \uparrow\rangle_r)$ where $|\alpha| = |\beta| = 1/\sqrt{2}$, the entanglement fidelity is given by

$$\begin{aligned}
\mathcal{F}_r^{\text{theory}} &\equiv \frac{\langle \psi_{\text{ideal}} | \rho_{\text{out}} | \psi_{\text{ideal}} \rangle}{\text{Tr}(|\psi_{\text{out}}\rangle \langle \psi_{\text{out}}|)} = \frac{|\alpha|^4 E_{\pi}^4(\rho_1^1, \rho_1^4) + |\beta|^4 |r_1^l|^2 E_{\pi}^1(\rho_4^4, \rho_4^1) - |\alpha^* \beta|^2 r_1^l E_{\pi}^3(\rho_2^2, \rho_2^3) - |\alpha \beta^*|^2 r_1^{l*} E_{\pi}^2(\rho_3^3, \rho_3^2)}{|\alpha|^2 E_{\pi}^4(\rho_1^1, \rho_1^4) + |\beta|^2 |r_1^l|^2 E_{\pi}^1(\rho_4^4, \rho_4^1) + |\alpha|^2 E_{\pi}^1(\rho_1^4, \rho_1^1) + |\beta|^2 |\hat{r}_1^l|^2 E_{\pi}^4(\rho_1^4, \rho_1^4)} \\
&\approx_{\substack{r_1^l = -1 \\ \hat{r}_1^l = 0}} 1 - \frac{5\pi}{4} \left(\frac{\kappa + \gamma_r}{\Omega_r} \right) - \frac{3}{2} \frac{1}{\Omega_r^2 T_2^{*2}}, \quad (35)
\end{aligned}$$

for $\kappa \ll \Omega_r$ where $\Omega_r T_{\pi} = \pi$ for a π -pulse. The final expression is found by perturbative expansion for each error to the first order. Using the relevant parameters: $T_{\pi} = 7$ ns, $T_{\pi/2} = 3.5$ ns, $\kappa = 0.0098$ ns $^{-1}$, $\gamma_r = 0.0081$ ns $^{-1}$ and $T_2^* = 23.2$ ns, we find $\mathcal{F}_{\kappa}^{\text{theory}} = 84.6\%$ from the analytical form in Eq. (35) taking $r_1 = -1$ and $\hat{r}_1 = 0$.

6. Spin readout error

The non-ideal spin readout by optical pumping is also considered to be one of the dominant sources of imperfections as it directly influences the spin readout basis. Due to finite optical cyclicity, optically pumping of the main transition can unfavourably result in an opposite outcome by flipping the spin state:

$$\rho_{\text{out}} \xrightarrow{\text{Spin readout}} \mathcal{F}_R \rho_{\text{out}} + (1 - \mathcal{F}_R) \hat{\sigma}_x(\pi) \rho_{\text{out}} \hat{\sigma}_x^{\dagger}(\pi). \quad (36)$$

where the readout fidelity is estimated to be $\mathcal{F}_R = 96.6\%$ [16]. Using Eqs. (33) and (36), the resulting entanglement fidelity under both rotation error and imperfect spin readout is $\mathcal{F}_{\kappa,R}^{\text{theory}} = (81.8 \pm 0.6)\%$. From here it is apparent that the dominant infidelity results from incoherent spin flips κ and finite γ_r (15.4%).

7. Driving-induced dephasing due to multi-photon scattering

Another source of error originates from the finite multi-photon component of the input pulse, which destroys the QD ground-state spin coherence through successions of photon-scattering events within the pulse. The driving-induced dephasing probability p_d is related to the success probability of scattering $P_{\omega_1} + P_{\omega_2}$ and the mean photon number in the driving pulse \bar{n} via $p_d = 1 - \exp[-\bar{n}(P_{\omega_1} + P_{\omega_2})]$ [17]. This can be understood as the probability of \bar{n} disjoint successful scattering events. To describe the effect of this error, we adopt a phase-damping model \mathcal{E}_d where

$$\mathcal{E}_d\left(\text{Tr}_p(\hat{S}(\rho_p \otimes \rho_s))\right) \equiv \left(1 - \frac{p_d}{2}\right) \text{Tr}_p(\hat{S}(\rho_p \otimes \rho_s)) + \frac{p_d}{2} \hat{\sigma}_z \text{Tr}_p(\hat{S}(\rho_p \otimes \rho_s)) \hat{\sigma}_z^\dagger = \begin{bmatrix} s_{11} & (1-p_d)s_{12} \\ (1-p_d)s_{21} & s_{22} \end{bmatrix}. \quad (37)$$

Here \hat{S} is the scattering matrix acting on the spin-photon density matrix and s_{ij} corresponds to the (i, j) -th entry of the reduced spin density matrix $\text{Tr}_p(\hat{S}(\rho_p \otimes \rho_s))$. \mathcal{E}_d introduces dephasing only to the QD spin state thus the photonic component is traced out before applying the phase-damping channel. Now we follow the same approach in Sec. D 5 and consider propagation of the dephasing error in the protocol:

$$\begin{aligned} \rho_p \otimes \rho_s &\xrightarrow{\hat{R}_y(\pi/2)} \begin{bmatrix} |\alpha|^2 & \alpha^* \beta \\ \alpha \beta^* & |\beta|^2 \end{bmatrix} \otimes \frac{1}{2} \begin{bmatrix} 1 & 1 \\ 1 & 1 \end{bmatrix} \\ &\xrightarrow{\mathcal{E}_d(\hat{S}_e)} \frac{1}{2} \begin{bmatrix} |\alpha|^2 \mathcal{E}_d \left(\begin{bmatrix} |r_1^e|^2 & r_1^{e*} \hat{r}_1^e \\ r_1^e \hat{r}_1^{e*} & |\hat{r}_1^e|^2 \end{bmatrix} \right) & \alpha^* \beta \mathcal{E}_d \left(\begin{bmatrix} r_1^{e*} & r_1^{e*} \\ \hat{r}_1^{e*} & \hat{r}_1^{e*} \end{bmatrix} \right) \\ \alpha \beta^* \mathcal{E}_d \left(\begin{bmatrix} r_1^e & \hat{r}_1^e \\ r_1^e & \hat{r}_1^e \end{bmatrix} \right) & |\beta|^2 \mathcal{E}_d \left(\begin{bmatrix} 1 & 1 \\ 1 & 1 \end{bmatrix} \right) \end{bmatrix} \\ &\xrightarrow{\hat{R}_y(\pi)} \frac{1}{2} \begin{bmatrix} |\alpha|^2 \begin{bmatrix} |\hat{r}_1^e|^2 & -(1-p_d)r_1^e \hat{r}_1^{e*} \\ -(1-p_d)r_1^{e*} \hat{r}_1^e & |r_1^e|^2 \end{bmatrix} & \alpha^* \beta \begin{bmatrix} \hat{r}_1^{e*} & -(1-p_d)\hat{r}_1^{e*} \\ -(1-p_d)r_1^{e*} & r_1^{e*} \end{bmatrix} \\ \alpha \beta^* \begin{bmatrix} \hat{r}_1^e & -(1-p_d)\hat{r}_1^e \\ -(1-p_d)r_1^e & r_1^e \end{bmatrix} & |\beta|^2 \begin{bmatrix} 1 & -(1-p_d) \\ -(1-p_d) & 1 \end{bmatrix} \end{bmatrix} \\ &\xrightarrow{\mathcal{E}_d(\hat{S}_l)} \frac{1}{2} \begin{bmatrix} |\alpha|^2 \begin{bmatrix} |\hat{r}_1^e|^2 & -(1-p_d)^2 r_1^e \hat{r}_1^{e*} \\ -(1-p_d)^2 r_1^{e*} \hat{r}_1^e & |r_1^e|^2 \end{bmatrix} & \alpha^* \beta \begin{bmatrix} r_1^l \hat{r}_1^{e*} & -(1-p_d)^2 \hat{r}_1^l \hat{r}_1^{e*} \\ -(1-p_d)^2 r_1^l r_1^{e*} & \hat{r}_1^l r_1^{e*} \end{bmatrix} \\ \alpha \beta^* \begin{bmatrix} r_1^{l*} \hat{r}_1^e & -(1-p_d)^2 r_1^{l*} r_1^e \\ -(1-p_d)^2 \hat{r}_1^{l*} \hat{r}_1^e & \hat{r}_1^{l*} r_1^e \end{bmatrix} & |\beta|^2 \begin{bmatrix} |r_1^l|^2 & -(1-p_d)^2 r_1^{l*} \hat{r}_1^l \\ -(1-p_d)^2 r_1^l \hat{r}_1^{l*} & |\hat{r}_1^l|^2 \end{bmatrix} \end{bmatrix}. \quad (38) \end{aligned}$$

Similarly, the entanglement fidelity under the driving-induced dephasing is found to be

$$\mathcal{F}_r^{\text{theory}} = \frac{\frac{1}{2}|r_1|^2 [1 + e^{-2\bar{n}(P_{\omega_1} + P_{\omega_2})}]}{|r_1|^2 + |\hat{r}_1^e|^2} \xrightarrow{r_1 \rightarrow -1, \hat{r}_1 \rightarrow 0} \frac{1}{2} [1 + e^{-2\bar{n}(P_{\omega_1} + P_{\omega_2})}] \approx 1 - \bar{n}(P_{\omega_1} + P_{\omega_2}), \quad (39)$$

where the average probability of successful scattering is given by Eq. (4):

$$P_{\omega_1} + P_{\omega_2} = \int_{-\infty}^{\infty} \left[|r_1(\omega)|^2 + |t_1(\omega)|^2 + |r_2(\omega)|^2 + |t_2(\omega)|^2 \right] |\Phi_1(\omega)|^2 d\omega. \quad (40)$$

To estimate the infidelity in the experiment, we first extract the average number of photons in the pulse $\bar{n} \leq (0.089 \pm 0.012)$ (Supplementary Note 5). Given that optical cyclicity $C = 14.7$, pulse bandwidth $\sigma_o = \sqrt{2 \ln 2} / T_{\text{FWHM}} \approx 0.589 \text{ ns}^{-1}$, spectral diffusion fluctuation $\sigma_e = 2\pi \times (332 \pm 15) \text{ MHz}$ and waveguide coupling efficiency $\beta \geq 0.865 \pm 0.059$ (Supplementary Note 4), the experimental infidelity is estimated using the exact form in Eq. (39) to be $1 - \mathcal{F}_{\bar{n}}^{\text{theory}} \leq (7.2 \pm 0.7)\%$.

E. Estimate the Overall Entanglement Fidelity

Assuming perfect manipulation of the hole spin state, the entanglement fidelity is expressed by:

$$\mathcal{F}_r^{\text{theory}} = 1 - \frac{\gamma_d}{\Gamma} - \frac{\Gamma^2}{4\Delta_h^2} \left(\frac{C}{C+1} \beta \right)^2 \approx 1 - \frac{\gamma_d}{\Gamma} - \frac{\Gamma^2}{4\Delta_h^2}, \quad (41)$$

which is estimated to be $(96.2 \pm 0.1)\%$ with $\Gamma = 2.48 \text{ ns}^{-1}$, $\Delta_h = 2\pi \times 7.3 \text{ GHz}$ [6] and $\gamma_d = (0.099 \pm 0.004) \text{ ns}^{-1}$ (Supplementary Note 3). This predominantly reflects the infidelity from phonon-induced pure dephasing $1 - \mathcal{F}_{\gamma_d}^{\text{theory}}$ as the off-resonant reflection error Γ^2/Δ_h^2 is comparably small. Together with the incoherent spin-flip, driving-induced dephasing and the readout errors discussed above, we estimate a lower bound on the overall entanglement fidelity $\mathcal{F}_{\text{total}}^{\text{theory}}$ of

$$\mathcal{F}_{\text{total}}^{\text{theory}} \approx \mathcal{F}_{\gamma_d}^{\text{theory}} \times \mathcal{F}_{\kappa, R}^{\text{theory}} \times \mathcal{F}_{\bar{n}}^{\text{theory}} \approx (73.0 \pm 0.6)\%, \quad (42)$$

which generally agrees with the experimentally obtained value $(74.3 \pm 2.3)\%$ including error margins. Here a lower fidelity bound is obtained as the waveguide-coupling efficiency β could be underestimated (Supplementary Note 4) which leads to overestimating \bar{n} and the corresponding infidelity $1 - \mathcal{F}_{\bar{n}}^{\text{theory}}$. Imperfect spin initialization (1.4%) [13] is not considered in the theory but is expected to have negligible infidelity ($< 1\%$).

SUPPLEMENTARY NOTE 3: PHOTON VISIBILITY AND PURE DEPHASING RATE ESTIMATION

Here we derive an analytical form of the visibility as a function of the QD pure dephasing rate. In the experiment, a time-bin encoded qubit (a weak coherent state) is scattered by a QD spin embedded in a two-sided photonic-crystal waveguide, and is subsequently measured by an asymmetric Mach-Zehnder interferometer with equal time delay as the qubit. The visibility is therefore a measure of the temporal overlap between the time-bins of the scattered pulses. To model this, we consider the scattering of the time-bin photon with the QD and project the output state onto the photonic X-bases. The initial state of the system is expressed as $|\text{in}\rangle = (|e\rangle + |l\rangle)/\sqrt{2} \otimes |\uparrow\rangle$. Here we have neglected the multi-photon components from the coherent state since we are interested in the effect of pure dephasing. For a complete modelling of the photon visibility, however, one should include the effect of multi-photon scattering and inelastic contributions [18].

With Eq. (4) the output state becomes

$$|\text{out}\rangle = \frac{1}{\sqrt{2}} \left[r_1 \left(|e\rangle_r + |l\rangle_r \right) + t_1 \left(|e\rangle_t + |l\rangle_t \right) \right] \otimes |\uparrow\rangle + \frac{1}{\sqrt{2}} \left[r_2 \left(|e'\rangle_r + |l'\rangle_r \right) + t_2 \left(|e'\rangle_t + |l'\rangle_t \right) \right] \otimes |\downarrow\rangle, \quad (43)$$

where the superscript prime ($'$) represents a scattered photon of frequency $\omega_2 \neq \omega_1$ and the subscript “r” (“t”) indicates a reflected (transmitted) photon. We then seek the photonic density matrix by tracing out the spin degree of freedom, the transmitted photons as well as the wrong frequency state ω_2 . For ease of computation the scattering coefficients are replaced by C_i where i refers to the time-bin, thus

$$|\text{out}\rangle_{\text{p}} \langle \text{out}|_{\text{p}} = \frac{\text{Tr}_{s,t,\omega}(|\text{out}\rangle \langle \text{out}|)}{\text{Tr}(|\text{out}\rangle \langle \text{out}|)} = |C_e|^2 |e\rangle \langle e| + |C_l|^2 |l\rangle \langle l| + C_e C_l^* |e\rangle \langle l| + C_l C_e^* |l\rangle \langle e|. \quad (44)$$

Now Eq. (44) is used to evaluate the middle-bin intensity in detector D2(D1):

$$I_{\text{D2/D1}} = \int \text{Tr} \left[\frac{(\hat{a}_e \pm e^{i\theta_p} \hat{a}_l)}{\sqrt{2}} \left(|\text{out}\rangle_{\text{p}} \langle \text{out}|_{\text{p}} \right) \frac{(\hat{a}_e^\dagger \pm e^{-i\theta_p} \hat{a}_l^\dagger)}{\sqrt{2}} \right] dt, \quad (45)$$

where the output photon state is projected onto the superposition state $\hat{a}_e(t) \pm e^{i\theta_p} \hat{a}_l(t)$ which is equivalent to adding a phase shifter on the long path of the excitation interferometer and interfering both bins. Setting $\theta_p = 0$ implies projecting the output state into the $p_{\pm} = |\pm X\rangle_{\text{p}} \langle \pm X|_{\text{p}}$ bases as described in the main text. The projected state is then traced out in both the early and late time bases. The photon visibility is defined as the normalized contrast of the middle-bin intensity when $\theta_p = 0$:

$$V_p \equiv \frac{I_{\text{D2}} - I_{\text{D1}}}{I_{\text{D2}} + I_{\text{D1}}} = \frac{\int \text{Tr} \left(\hat{a}_e |\text{out}\rangle_{\text{p}} \langle \text{out}|_{\text{p}} \hat{a}_l^\dagger + \hat{a}_l |\text{out}\rangle_{\text{p}} \langle \text{out}|_{\text{p}} \hat{a}_e^\dagger \right) dt}{\int \text{Tr} \left(\hat{a}_e |\text{out}\rangle_{\text{p}} \langle \text{out}|_{\text{p}} \hat{a}_e^\dagger + \hat{a}_l |\text{out}\rangle_{\text{p}} \langle \text{out}|_{\text{p}} \hat{a}_l^\dagger \right) dt}. \quad (46)$$

To further simplify the above expression, we consider the scattering events of the early and late bins to be identical, i.e., with the same scattering coefficient $C_e = C_l = r_1$. as justified in Sec. D4. Therefore, under this assumption the photon visibility becomes unity in the single-photon regime.

Following from the discussion in Sec. D3, we can now account for the effect of phonon-induced pure dephasing [10]. In essence, the resulting spin-photon density matrix is the sum of coherent and incoherent parts as described by Eqs. (15) and (16). The advantage of the formalism in Eq. (15) is that its effect can be straightforwardly included in Eq. (44). Accordingly, the new photonic density matrix becomes

$$|\text{out}'\rangle_{\text{p}} \langle \text{out}'|_{\text{p}} \approx |\text{out}\rangle_{\text{p}} \langle \text{out}|_{\text{p}} + \frac{1}{2} P_{\gamma_d}^{\omega_1} \rho_{\gamma_d,e}^{\omega_1} |\emptyset\rangle_l \langle \emptyset|_l + \frac{1}{2} P_{\gamma_d}^{\omega_1} \rho_{\gamma_d,l}^{\omega_1} |\emptyset\rangle_e \langle \emptyset|_e, \quad (47)$$

where the last two terms correspond to dephasing occurred during the single-photon scattering of either the early or late time-bin. The effect of pure dephasing on the multi-photon component is not considered due to its polynomial dependence on the mean photon number per pulse \bar{n} , which is negligible as $\bar{n} \ll 1$. Note that the incoherent photon does not contribute to the interference since $\text{Tr} \left(\hat{a}_e \rho_{\gamma_d,e}^{\omega_1} |\emptyset\rangle_l \langle \emptyset|_l \hat{a}_l^\dagger \right) = \text{Tr} \left(\hat{a}_e \rho_{\gamma_d,e}^{\omega_1} \right) \times \text{Tr} \left(|\emptyset\rangle_l \langle \emptyset|_l \hat{a}_l^\dagger \right) = 0$. This means only the total intensity is affected and Eq. (46) can be simplified as

$$V_p = \frac{\int_{-\infty}^{\infty} |\Phi_1(\omega)|^2 |r_1(\omega)|^2 d\omega}{\int_{-\infty}^{\infty} |\Phi_1(\omega)|^2 |r_1(\omega)|^2 d\omega + P_{\gamma_d}^{\omega_1}}. \quad (48)$$

To include slow resonance drift $\omega \rightarrow \omega + \delta_e$ due to spectral wandering, both the probability of reflecting a photon $\int_{-\infty}^{\infty} |\Phi_1(\omega)|^2 |r_1(\omega)|^2 d\omega$ and the pure dephasing probability $P_{\gamma_d}^{\omega_1}$ need to be averaged over a Gaussian distribution $N(0, \sigma_e)$:

$$N(0, \sigma_e) = \frac{1}{\sqrt{2\pi\sigma_e^2}} e^{-\frac{\delta_e^2}{2\sigma_e^2}}, \quad (49)$$

with standard deviation of the drift σ_e [19]. Eq. (16) is then rewritten as

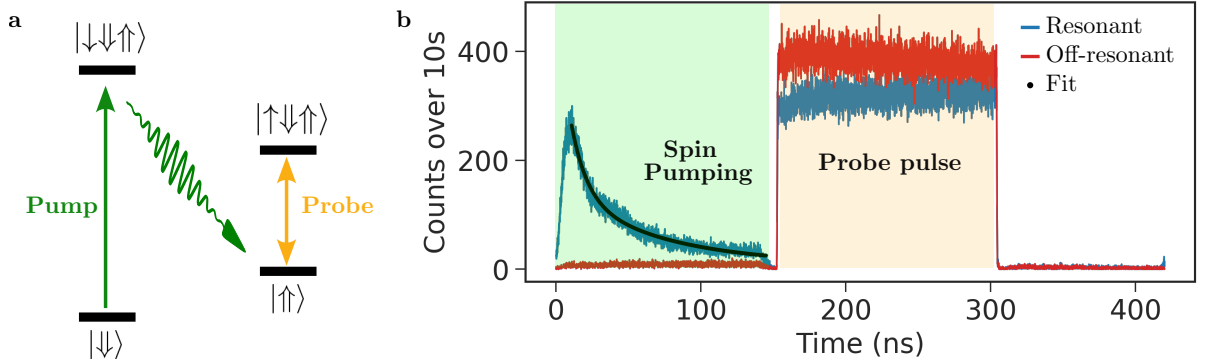
$$P_{\gamma_d}^{\omega_1} = \frac{\Gamma_1^r}{\Gamma} P_{\gamma_d} = \frac{\Gamma_1^r}{\Gamma} \int_{-\infty}^{\infty} \int_{-\infty}^{\infty} \frac{e^{-\frac{(\omega-\omega_1)^2}{2\sigma_e^2}}}{\sqrt{2\pi\sigma_e^2}} \left| \frac{-2\sqrt{2\gamma_d}\Gamma_1^r}{\Gamma + 2i(\omega - \omega_1 + \delta_e)} \right|^2 N(0, \sigma_e) d\omega d\delta_e, \quad (50)$$

and Eq. (48) becomes

$$V_p = \frac{\int_{-\infty}^{\infty} \int_{-\infty}^{\infty} |\Phi_1(\omega)|^2 |r_1(\omega)|^2 N(0, \sigma_e) d\omega d\delta_e}{\int_{-\infty}^{\infty} \int_{-\infty}^{\infty} |\Phi_1(\omega)|^2 |r_1(\omega)|^2 N(0, \sigma_e) d\omega d\delta_e + P_{\gamma_d}^{\omega_1}} = \frac{\Gamma}{\Gamma + 2\gamma_d}, \quad (51)$$

which is interestingly identical to the photon indistinguishability formula derived in Ref. [10]. In the limit $\bar{n} \approx 0$ where only single photons interact with the QD, the y -intercept of the photon visibility curve in Figure 2b of the main text is therefore given by Eq. (51). A linear fit followed by extrapolation of the data gives a y -intercept of $V_p = 0.926 \pm 0.003$ implying $\gamma_d \approx (0.099 \pm 0.004) \text{ ns}^{-1}$. V_p can be intuitively understood as the mean wavepacket overlap between single photons.

SUPPLEMENTARY NOTE 4: TWO-COLOR TRANSMISSION EXPERIMENT

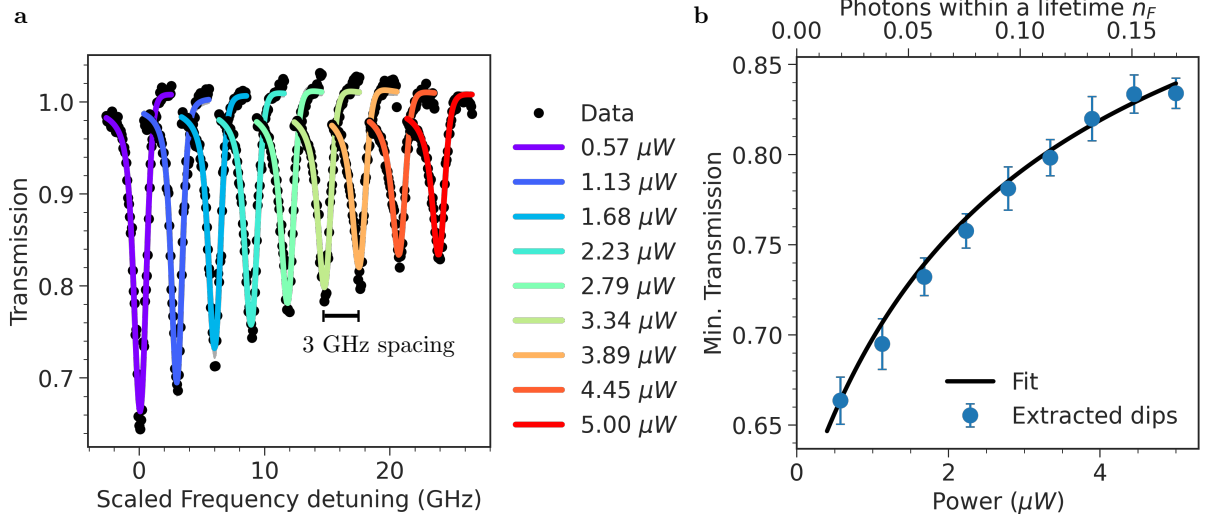


Supplementary Figure 3. Two-color transmission measurement on the waveguide-embedded QD hole spin. (a) QD Level diagram. A strong pump pulse (green) prepares the spin state $|\uparrow\uparrow\rangle$, while the frequency of the weak probe pulse (orange) is scanned to reveal the QD transmission spectrum. (b) Time-resolved histogram of the pulse sequence with resonant (1.148 V) and off-resonant (1 V) bias voltages. A bi-exponential fit is used to extract a lower bound on the spin pumping fidelity.

To probe the photon-emitter coupling efficiency of the device and spectral diffusion noise of the QD spin, we perform a series of spin-dependent transmission measurements at various powers of the probe laser. The experiment is conducted by first initializing the QD spin in the $|\uparrow\uparrow\rangle$ state, followed by scanning the frequency of a 150-ns probe pulse at a given power (Supplementary Figure 3). Since the probe is orders of magnitude longer than the QD lifetime, the atom saturates similarly as being driven by a continuous-wave laser. The destructive interference between the phase-shifted scattered light and the probe in the waveguide results in a transmission dip on resonance [19, 20], where the shape of the transmission spectrum is determined by the combination of phonon-induced pure dephasing γ_d , coupling efficiency β , spectral diffusion σ_e , Fano parameter ξ , laser power P and cyclicity C . In particular, the normalized transmission function used to fit the data is given by

$$\mathcal{I}_T(\omega - \omega_1) = 1 + P_{sp} \times \text{Re} \left(\frac{\frac{C}{C+1} \beta \Gamma^2 [\Gamma + 2\gamma_d + 2i(\omega - \omega_1)] (i + \xi) [2i + \frac{C}{C+1} \beta (-i + \xi)]}{\Gamma [(\Gamma + 2\gamma_d)^2 + 4(\omega - \omega_1)^2] + 8\eta(\Gamma + 2\gamma_d)P} \right). \quad (52)$$

Here P_{sp} represents the spin pumping fidelity. A non-unity P_{sp} implies the QD could go dark when its spin is prepared in the wrong state [21]. An average value for P_{sp} is obtained by first fitting the fluorescence decay during the pumping pulse (Supplementary Figure 3b) then averaging over all frequencies and probe powers. In the low power limit $P \rightarrow 0$ with a perfectly prepared two-level system $P_{sp} \rightarrow 1$, the expression reduces to Eq. (S33) in Ref. [19] with β replaced by $\frac{C}{C+1}\beta$, as a finite C limits the number of resonantly reflected photons leading to diminished interference. To take slow resonance drifts due to spectral diffusion into account, $\mathcal{I}_T(\omega - \omega_1)$ is averaged over the Gaussian distribution $N(0, \sigma_e)$ (Supplementary Note 3).



Supplementary Figure 4. Results from iteratively fitting transmission spectra to extract coupling efficiency β and spectral diffusion σ_e . (a) Transmission spectra fitted at different probe powers. The frequency detuning axis has been rescaled such that each spectra is 3 GHz apart. The central frequency is 317.235 THz. The data (black circles) are fitted using Eqs. (49) and (52). (b) The transmission dips extracted from (a) are then fitted to estimate β .

We have developed an iterative fitting procedure for the data in Supplementary Figure 4 to reliably estimate β and σ_e . The general idea is to divide the data into two sub-dataset and fit both on each iteration. The first dataset is a set of transmission spectra as a function of probe powers, while the second dataset consists of only the transmission dip at various powers. The algorithm runs iteratively based on results from the previous fit and terminates when the fitted parameters from both fits converge. The convergence implies that there is a set of parameters which simultaneously holds true when using two different fit functions on the same data.

The fitting process is described as follows: (1) We fix the total decay rate $\Gamma = 2.48 \text{ ns}^{-1}$ [13], $P_{sp} = 0.897$, $\gamma_d = 0.099 \text{ ns}^{-1}$ and $C = 14.7$ [13] as they are measured independently. For the first fit we assume $\beta = 0.95$; (2) Based on these values, we take σ_e , ξ and loss factor η as free parameters to perform a least square fit on the transmission spectrum at each power (Supplementary Figure 4a). This results in a list of fitted values for σ_e , ξ and η . Their corresponding mean values are then used to fit the second dataset (transmission dips as a function of probe power) with only β and η as free parameters (Supplementary Figure 4b). (3) From here we obtain an updated value of β which is used to fit the transmission spectra again in step 2. (4) The iteration stops when β after loop i converges (i.e., $|\beta_i - \beta_{i-1}| < 0.1\%$).

Parameter	Value	Confidence interval (99.7%)
β	0.865	[0.806, 0.924]
$\sigma_e/2\pi$	332 MHz	[317, 347]
η	0.427	[0.406, 0.448]
ξ	-0.127	[-0.136, -0.118]
P_{sp}	0.897	[0.895, 0.899]

Supplementary Table 1. Relevant parameters extracted from fitting the transmission spectra.

The fit is completed in 10 iterations. The extracted parameters with 3σ -uncertainty are presented in Supplementary Table 1. Both $\sigma_e = 2\pi \times (332 \pm 15)$ MHz and $\beta = (0.865 \pm 0.059)$ are in very good agreement with previous estimates from two-color continuous-wave pumping resonance fluorescence [6] and transmission [19] measurements, respectively,

indicating that the combination of two-color pulsed transmission and photon visibility measurements through QD scattering in the waveguide could be an alternative way to accurately extract these QD noise parameters. Note that due to the non-unity hole initialization efficiency, the actual value of β could be even higher, as the QD also blinks if the hole spin is not loaded. Additionally, since the pumping pulse is generated with a slow acousto-optical modulator with 8 ns rise time, the imperfect pump pulse shape together with residual repumping from the probe pulse might have underestimated the spin pumping fidelity. Therefore, the extracted value of $\beta = (0.865 \pm 0.059)$ constitutes a lower bound.

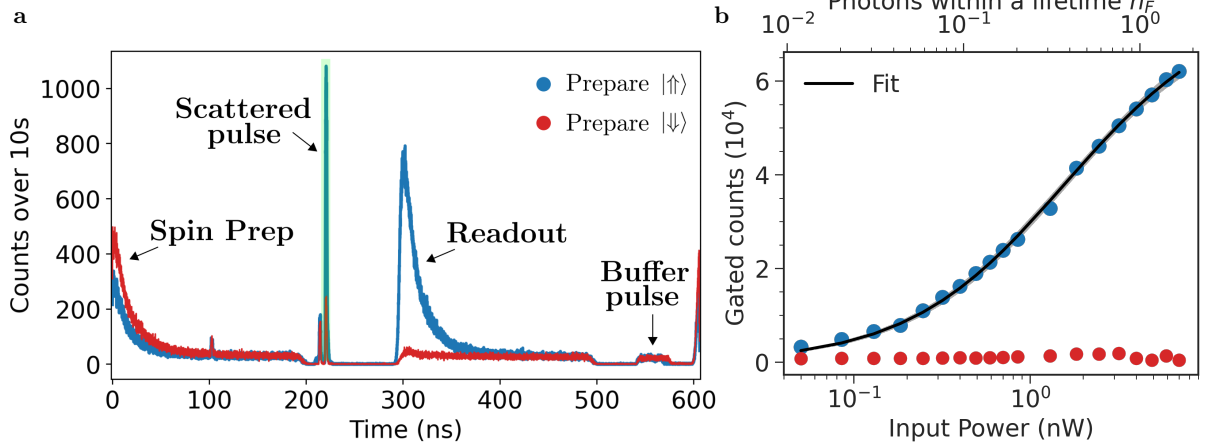
The conversion between the probe power and the mean photon number *within* a QD lifetime n_F in Supplementary Figure 4b is obtained using Eq. (53) and the extracted values for η , σ_e , β (Supplementary Table 1) and γ_d . The transmission spectrum in Figure 1c (in the main text) is probed at an input power of $P = 0.57 \mu\text{W}$, with the saturation parameter $S = 0.054$ corresponding to an average of $n_F = 0.02 \ll 1$ photons interacting with the QD within its lifetime.

SUPPLEMENTARY NOTE 5: SPIN-DEPENDENT REFLECTIVITY MEASUREMENT

Apart from measuring the photon visibility, another approach to probe the single-photon nature of the scattering process is through QD saturation measurement, in which the QD response is observed by scanning the power of the input qubit laser. From fitting the scattered signal, the mean photon number per pulse \bar{n} can be extracted, where $\bar{n} \ll 1$ indicates the scattering occurs in the single-photon regime. To mimic the entanglement experiment, we prepare a single pulse of 2 ns duration and scatter on a QD spin initialized in either $|\uparrow\rangle$ or $|\downarrow\rangle$. Due to the QD spin-dependent reflectivity, the input photon which is resonant with the QD transition $|\uparrow\rangle \rightarrow |\uparrow\downarrow\uparrow\rangle$ is coherently reflected. By time-gating on the reflected signal (Supplementary Figure 5a; green shaded region) and increasing the input power, the QD prepared in $|\uparrow\rangle$ becomes saturated (Supplementary Figure 5b). The averaged intensity in the reflected signal is fitted assuming a two-level system between $|\uparrow\rangle \rightarrow |\uparrow\downarrow\uparrow\rangle$:

$$\mathcal{I}_R = \mathcal{I}_{\max} \int_{-\infty}^{\infty} \frac{\frac{C}{C+1} \beta (1 + \frac{2\gamma_d}{\Gamma}) \Omega_1^2}{(\frac{\Gamma}{2} + \gamma_d)^2 + \delta_e^2 + 2(1 + \frac{2\gamma_d}{\Gamma}) \Omega_1^2} N(0, \sigma_e) d\delta_e, \quad (53)$$

where Ω_1 is the Rabi frequency driving the transition $|\uparrow\rangle \rightarrow |\uparrow\downarrow\uparrow\rangle$, δ_e is the effective resonance drift due to spectral diffusion. A setup loss factor η is introduced to associate the Rabi frequency to the input power P where $\Omega_1 = \sqrt{\eta P}$. Here \mathcal{I}_{\max} and η are free parameters, whereas σ_e and γ_d are fitted in Supplementary Note 4. Eq. (53) holds when



Supplementary Figure 5. Saturation measurement to calibrate the mean photon flux. (a) Time-resolved histogram of the measurement sequence. A 2 ns pulse gets reflected from a QD prepared in $|\uparrow\rangle$ via optical spin pumping followed by a π -rotation pulse. The reflected signal is time-gated (green shaded region) and recorded for each input power. Peaks at around 100 and 215 ns are laser scatter from the time-bin interferometer and the optical breadboard respectively. The spin readout at 300 ns maintains the same duty cycle as the entanglement experiment and does not affect the gated counts. (b) Gated fluorescence in the reflection as a function of the input pulse power. Blue (red) circles are summed counts over a time window of 3 ns, when the QD spin is prepared in $|\uparrow\rangle$ ($|\downarrow\rangle$). Fitted (black solid line) using Eq. (53). Around 0.075 nW is used for a single pulse in the entanglement experiment.

$\Gamma \gg \kappa_g$ and $T_p \gg \Gamma^{-1}$ where κ_g is the effective spin-flip rate between the hole ground states and T_p is the FWHM

qubit duration measured from the pulse intensity. The first condition implies that the main transition is eventually saturated as the QD decays faster than the spin can recycle, thus $|\downarrow\rangle$ effectively becomes dark. This is generally true since κ_g is typically on the order of 10^{-7} ns^{-1} at the plateau center voltage [22], which is lower than $\Gamma = 2.48 \text{ ns}^{-1}$. The second condition ensures that the QD decays back to $|\uparrow\rangle$ before the next scattering event within the pulse. When the driving pulse is sufficiently long, i.e., $T_p = 2 \text{ ns} > \Gamma^{-1} = 0.4 \text{ ns}$ with increasing power, the QD saturates similarly as when being driven by a weak continuous-wave laser. In addition, a finite cyclicity leads to a resonant spin-flip into the dark state $|\downarrow\rangle$ reflecting a photon of frequency $\omega_2 \neq \omega_1$ which is filtered out, thus only reducing the total intensity included in \mathcal{I}_{max} and not affecting the scaling of Eq. (53).

From fitting the data (Supplementary Figure 5b), we extract $\eta = (3.00 \pm 0.07) \text{ ns}^{-2}/\text{nW}$. The saturation parameter S at an input power $P = 0.075 \text{ nW}$ used for a single pulse is estimated to be 0.05 ± 0.001 using

$$S = \int_{-\infty}^{\infty} \frac{2(1 + \frac{2\gamma_d}{\Gamma})\eta P}{(\frac{\Gamma}{2} + \gamma_d)^2 + \delta_e^2} N(0, \sigma_e) d\delta_e. \quad (54)$$

The mean photon number *within* QD lifetime or mean photon flux is defined as $n_F \equiv S n_c$ with $n_c \equiv (1 + 2\gamma_d/\Gamma)/4\beta^2$ to be the critical photon flux leading to an excited state population of $1/4$. As a sanity check, in the ideal limit where $\gamma_d, \delta_e \rightarrow 0$ and $\beta \rightarrow 1$, $n_F = 2\Omega_1^2/\Gamma^2$ which recovers the definition in Ref. [20]. Using $\beta \geq 0.865 \pm 0.059$, we estimate the average number of photons in a single pulse $\bar{n} = n_F T_p \Gamma \leq 0.089 \pm 0.012 \ll 1$.

SUPPLEMENTARY NOTE 6: OPTICAL SPIN CONTROL AND ROTATION FIDELITY

In this section, we briefly summarize the principle of optical control of the hole spin ground states, followed by experimental characterization of Rabi flopping between the hole ground states to extract the π -rotation fidelity.

Principle of Optical Spin Control

Supplementary Figure 6b depicts the level scheme of a hole spin under an external in-plane magnetic field, under the driving of a bi-chromatic laser. To optically drive the spin transitions, we employ a monochromatic laser (green) at a frequency $\omega_o = \omega_1 - \Delta_r$ detuned from the main transition $|\uparrow\rangle \leftrightarrow |\uparrow\downarrow\rangle$. This laser is microwave-modulated resulting in two sidebands at $\omega_o \pm \Delta_h/2$, where the higher-frequency (lower-frequency) band drives the $|\downarrow\rangle$ ($|\uparrow\rangle$) state. The combination of both colors drives both Λ -systems (labelled as “1” and “2”) via two-photon Raman transitions without populating the trions, thus creating an effective coupling between only the hole ground-state manifold.

For this two-photon Raman scheme to work [13, 15], each frequency band must be circularly-polarized, such that (1) it drives both vertical Y-polarized and diagonal X-polarized transitions with equal optical Rabi frequencies ($\Omega_y = \Omega_x$), and (2) Ω_x is $\pi/2$ out of phase with Ω_y , thus the optical fields constructively drive both Λ -systems. Intuitively, this could be visualized as reversing the direction of the arrows for diagonal transitions in Supplementary Figure 6b, where the Λ -system “1” (“2”) now transfers population from $|\downarrow\rangle$ to $|\uparrow\rangle$ ($|\uparrow\rangle$ to $|\downarrow\rangle$), forming a cycling drive via a virtual state.

Mathematically, the spin dynamics under the optical drive is governed by the effective spin TLS Hamiltonian [16]:

$$\hat{H}_s = \frac{\Omega_r}{2}(\hat{\sigma}_x \cos \phi_r + \hat{\sigma}_y \sin \phi_r) - \frac{\Delta_{\text{MW}}}{2}\hat{\sigma}_z, \quad (55)$$

where Ω_r is the effective spin Rabi frequency of the TLS. ϕ_r is the azimuthal angle on the Bloch sphere with hole spin states as the poles. $\phi_r = 0$ ($\phi_r = \pi/2$) sets the axis of rotation along $+x$ ($+y$). $\hat{\sigma}_i$ are Pauli matrices. Δ_{MW} is the detuning of the bi-chromatic laser with the virtual state. To study the time evolution of the hole spin state under Eq. (55), we refer to the Lindblad master equation ($\hbar = 1$):

$$\dot{\rho}_s = -i[\hat{H}_s, \rho_s] + \sum_{i=1}^n D[\hat{C}_i]\rho_s, \quad (56)$$

for ρ_s is the spin density matrix spanning the hole spin ground states. The latter term in Eq. (56) represents the static Lindblad dissipator $D[\hat{C}_i]\rho \equiv \hat{C}_i\rho\hat{C}_i^\dagger - \frac{1}{2}\{\hat{C}_i^\dagger\hat{C}_i, \rho\}$ for a list of n collapse operators \hat{C}_i . To model realistic noises in the experiment, we first consider a Markovian noise that destroys spin coherence by flipping the spin state with a rate κ . Specifically, we take $\hat{C}_1 = \sqrt{\kappa}\hat{\sigma}_+$ and $\hat{C}_2 = \sqrt{\kappa}\hat{\sigma}_-$ where $\hat{\sigma}_+ \equiv |\downarrow\rangle\langle\uparrow| = \hat{\sigma}_-^\dagger$ is the atomic raising operator.

Generally, for a finite detuning $\Delta_{\text{MW}} \neq 0$, Eq. (56) can only be numerically solved. To elaborate further, we now include the Overhauser field noise. For a frozen nuclear bath [12], this corresponds to introducing a fluctuating noise $\Delta_{\text{MW}} = \delta_g$ along z -axis of the spin Bloch sphere. The $|\downarrow\rangle$ population under such noise is then found by averaging $\rho_{|\uparrow\rangle\langle\uparrow|}(T_r, \delta_g)$ with a Gaussian spin dephasing profile $N(\delta_g, \sigma_{\text{OH}})$:

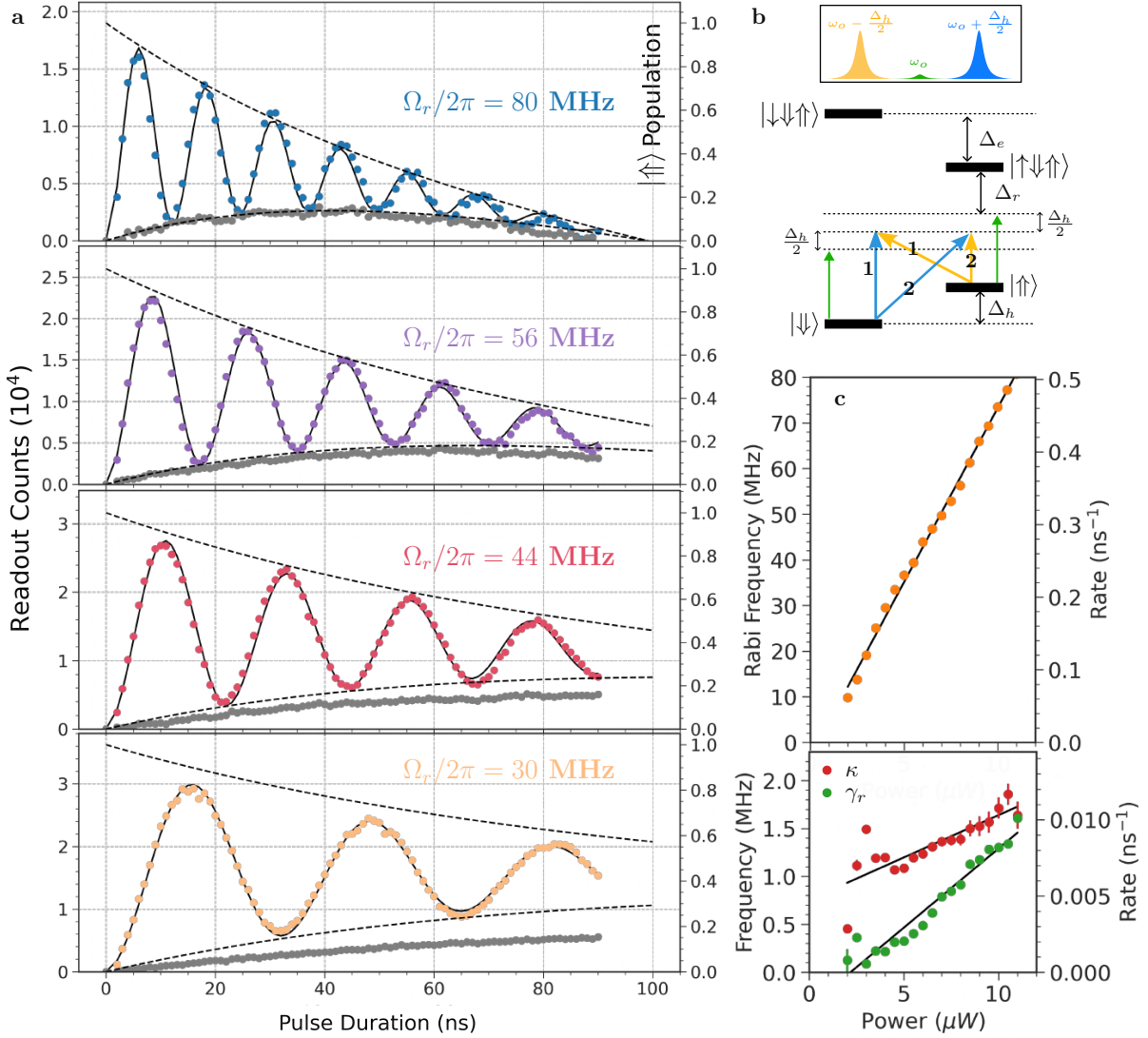
$$\bar{\rho}_{|\uparrow\rangle\langle\uparrow|}(T_r) = \int_{-\infty}^{\infty} d\delta_g \rho_{|\uparrow\rangle\langle\uparrow|}(T_r, \delta_g) N(\delta_g, \sigma_{\text{OH}}). \quad (57)$$

Measured Spin Rabi Oscillations

Supplementary Figure 6 shows measured and fitted Rabi oscillations between the hole spin ground states at different optical powers. To avoid populating the trion states, we set the carrier frequency ω_o of the Raman laser to be $\Delta_r = 2\pi \times 350$ GHz detuned from the main transition. The experiment begins by photocreating a hole spin with a 830 nm pulsed laser then optically pumping the hole spin into $|\downarrow\rangle$, followed by a pulse driven by the Raman laser with a varying duration T_r . The state evolution of the hole spin under the effect of Raman pulse is then probed by detecting fluorescence from $|\uparrow\rangle$ with a readout pulse. Note that a buffer pulse from the Raman laser is added at the end of the sequence, such that the sequence duty cycle and the average optical power of the laser are kept constant when sweeping T_r .

The fluorescence signal from the first 50 ns of the readout pulse can be fitted by the formula [16]:

$$I(T_r) = I_0 \times \eta_r \times \bar{\rho}_{|\uparrow\rangle\langle\uparrow|}(T_r), \quad (58)$$



Supplementary Figure 6. Rabi oscillations between the hole spin states. (a) Measured (dotted) and fitted (black lines) Rabi curves at different Raman laser powers. Dashed curves correspond to the κ -induced decay envelopes $\frac{1}{2}\eta_r(1 \pm e^{-3\kappa T_r/2})$. Grey curves are measured when the sidebands are off-resonant by $\Delta_{\text{MW}} = 2\pi \times 245$ MHz. (b) Schematics of optical spin control using a bi-chromatic laser assuming $\Delta_{\text{MW}} = 0$. (c) Power-dependence of the spin Rabi frequency Ω_r , spin-flip rate κ and γ_r .

where $\eta_r \approx (1 - \gamma_r T_r)$ is an empirical model describing the reduced readout efficiency with a power-dependent rate γ_r . Before fitting the data, the photon counts at $T_r = 0$ ns are first subtracted to remove background fluorescence from the readout pulse. Each dataset is numerically fitted with Eq. (58) using κ , γ_r , I_0 and Ω_r as free parameters, and with the standard deviation in Overhauser field fluctuations σ_{OH} fixed. The fitted peak intensity I_0 can then be extracted to normalize the dataset. For the fit, we take $\sigma_{\text{OH}} = \sqrt{2}/T_2^* \approx 2\pi \times 9.7$ MHz for a measured spin dephasing time of $T_2^* \approx 23.2$ ns [13]. In the limit of $\Omega_r > 5\sigma_{\text{OH}}$, the spin noise dynamics is dominated by κ as the curves in Supplementary Figure 6a become tightly bounded by the decay envelopes $\frac{1}{2}\eta_r(1 \pm e^{-3\kappa T_r/2})$.

Supplementary Figure 6c shows the fitted spin Rabi frequency Ω_r , the power-dependent spin-flip rate κ and γ_r , which all increase linearly with Raman laser power, as observed in Refs. [13, 15]. For modelling the entanglement infidelity due to imperfect spin rotations, we need to quantify the fidelity of the spin π -rotation F_π . For each normalized Rabi curve in Supplementary Figure 6a, F_π is estimated from its first peak at which the $|\uparrow\rangle$ population is maximized.

In the entanglement protocol experiment, a $T_r = 7$ ns π -pulse (corresponding to $\Omega_r \approx 71$ MHz) is used. Therefore, $F_\pi = (88.1 \pm 3.8)\%$ with $\kappa = (0.0098 \pm 0.0007)$ ns⁻¹ and $\gamma_r = (0.0081 \pm 0.0002)$ ns⁻¹, with error bounds obtained from the fit. The estimated rotation fidelity is consistent with the one extracted previously on the same QD ($F_\pi = (88.5 \pm 0.3)\%$) [13].

SUPPLEMENTARY NOTE 7: PROTOCOL PERFORMANCE METRICS

In this section we investigate the metrics that characterize the performance of the entanglement protocol. The protocol should operate at high speed, with a high fidelity, be tolerant to noise, and have low insertion loss. We estimate these metrics for our system to compare with the state-of-the-art photon-scattering protocols on other platforms in Supplementary Table 2.

Platform	Fidelity		Duration	Efficiency	Entanglement rate*	Ref.
	Raw	Corrected				
SiV-PCC	0.7	0.89-0.94	30 μ s	0.493	11.9 Hz	[23, 24]
QD-PCW	0.66	0.74	0.29 μ s	0.171	4.75 Hz	Present work
Rb-cavity	0.86 [†]	-	146 μ s	0.39	34.5 Hz	[25]

Supplementary Table 2. Comparison of various performance metrics. PCC: Photonic crystal cavity. PCW: Photonic crystal waveguide. *See Supplementary Table 4 for estimation details. [†]Not specified if raw or corrected.

From Supplementary Table 2, several conclusions can be drawn. First, the raw (corrected) entanglement fidelity 66% (74%) in QD-PCW is comparable to those achieved in SiV-PCC [23, 24]. It is noted that the 89% fidelity reported in Ref. [23] should be regarded as an inferred maximum fidelity after correcting for imperfect single-shot readout. In contrast our reported 74% fidelity only corrects for subtraction of background fluorescence due to time delay of rotational pulses in the long path of the interferometer (Supplementary Note 9), which can be readily mitigated using shorter pulses and better pulse shaping, or longer interferometric delays.

Second, the protocol duration of the QD-PCW is two-orders of magnitude shorter than that of SiV-PCC. This is primarily due to the long duration (30 μ s) required to distinguish between the two SiV spin states during single-shot readout [24]. Similarly the protocol duration is even longer in Rb-cavity system. Supplementary Table 3 shows a breakdown of the protocol duration, which is defined as the total duration of all pulses required to run the entanglement sequence. This includes the spin initialization pulse, two optical pulses with a delay that made up the photonic qubit, and the spin rotation $\pi/2$ - and π -pulses. For both systems, the emitter’s lifetime is short compared to the duration of each photonic pulse, and therefore not included in the protocol duration. A faster operating speed without compensating for entanglement fidelity therefore enables quantum communication at a higher clock rate.

Platform	Initialization	$2T_p$	TBI delay	$\pi/2$ -pulse	π -pulse	Ref.
SiV-PCC	30 μ s	20 ns	142 ns	16 ns	32 ns	[24]
SiV-PCC	13 μ s	10 ns	30 ns	6 ns	12 ns	[23]
QD-PCW	0.2 μ s	4 ns	11.8 ns	3.5 ns	7 ns	Present work
Rb-cavity	140 μ s	0.6 μ s*	-	1.7 μ s	3.4 μ s	[25]

Supplementary Table 3. Breakdown of the total protocol duration in each step. T_p : duration of a photonic pulse. TBI: time-bin interferometer. *The Rb-cavity scheme uses polarization-encoding for the photonic qubit.

For both schemes, the entanglement generation is conditioned on detecting a reflected photon, and is therefore ideally successful 50% of the time in each run since at most half of the input photon gets reflected when the spin is initialized in a superposition state. This means that the protocol success probability P_s depends on the spin-dependent reflectivity of the emitter, which can be expressed by Eq. (9):

$$P_s = \frac{1}{2} \left[\int_{-\infty}^{\infty} |\Phi_1(\omega)|^2 |r_1(\omega)|^2 d\omega + \int_{-\infty}^{\infty} |\Phi_1(\omega)|^2 |\hat{r}_1(\omega)|^2 d\omega + P_{\gamma_d}^{\omega_1} \right]. \quad (59)$$

We find that for each incoming photon, it is reflected with a probability of 33.9% from the $|\uparrow\rangle$ state and with a probability of 0.05% from $|\downarrow\rangle$. The protocol efficiency is therefore $(17.1 \pm 0.3)\%$. The reflectivity is inferred from the two-color transmission experiment (Supplementary Note 4), which depends on the device cooperativity and noise properties.

Another conclusion drawn from Supplementary Table 2 is that the entanglement rates of the QD-PCW and SiV-PCC systems are of similar order of magnitude despite the difference in efficiency. In our work, heralded spin readout is used instead since the single-shot fidelity could only reach 52% due to limited collection efficiency $\eta_c \approx 0.3\%$ and cyclicity $C = 14.7$ [13]. The collection efficiency can readily be improved in next-generation devices. The low coupling rate is compensated by the fast repetition rate of the system. As opposed to the 200 ms long calibration step, which includes active locking of the TBI and preselection procedures used to lock the SiV resonance, our experiment is able

to be executed in 606 ns. The self-stabilizing TBI in this work does not require active locking and offers week-long stability with $> 99\%$ interferometric visibility.

Platform	P_{photon} (%)	P_{spin} (%)	τ_{seq}	Entanglement rate
SiV-PCC	$2\langle n \rangle_m \eta = 0.17$	$F_{\text{ssr}} \eta = 42.3$	60 μs	11.9 Hz
QD-PCW	0.027	1.1	0.606 μs	4.75 Hz
Rb-cavity	$\langle n \rangle_m \eta = 3.45$	100	0.001 s	34.5 Hz

Supplementary Table 4. Entanglement rate estimation. P_{photon} (P_{spin}): probability of detecting a reflected photon during readout of the photonic (spin) qubit in a single run. τ_{seq} : sequence duration including spin initialization, protocol sequence and state readout. $\langle n \rangle_m$: average number of photon per pulse incident on the cavity. η : total heralding efficiency. F_{ssr} : fidelity of single-shot readout. For QD-PCW, P_{photon} (P_{spin}) is obtained by summing all photon clicks during the photonic (spin) detection windows, then divided by the 100 s integration time and repetition rate. For Rb-cavity, $\eta \equiv \mathcal{R} \eta_{\text{det}} = 0.69 \times 0.56 = 0.38$ and $\langle n \rangle_m = 0.09$.

In Supplementary Table 4 we estimate the entanglement rates of both systems using $\mathcal{R} \equiv P_{\text{photon}} \times P_{\text{spin}} \times \mathcal{R}_{\text{rep}}$ where the experimental repetition rate is given by $\mathcal{R}_{\text{rep}} = 1/\tau_{\text{seq}}$. P_{photon} (P_{spin}) is the probability of detecting a reflected photon in one iteration of the experiment during the photon (spin) readout window. For a fair comparison, we define τ_{seq} to be the time it takes to initialize, generate entanglement and read out the final state, rather than the total sequence time that includes calibration steps. To validate our rate estimation of 4.75 Hz, we predict an entanglement rate of $4.75 \text{ Hz} \times 4/(2\bar{n}) \approx 106 \pm 15 \text{ Hz}$ for Bell-state generation using optical excitations, where $2\bar{n} = 2 \times (0.089 \pm 0.012)$ is the total number of photons scattered off the QD and the factor of 4 originates from the 50% reduction in waveguide collection efficiency due to the cross-polarized scheme (Supplementary Note 1). This is in excellent agreement with 124 Hz extracted rate in Ref. [13]. A 25-fold improvement in the entanglement rate is possible as near-90% single-shot readout fidelity on a sub-nanosecond timescale with collection efficiency $\eta_c = 76\%$ can be achieved [26]. To reach an even higher entanglement rate, it is necessary to improve the device reflectivity by reducing the spectral diffusion noise and increasing the QD-waveguide coupling efficiency β .

SUPPLEMENTARY NOTE 8: CONCURRENCE ESTIMATE

Another measure frequently used in the literature to quantify entanglement is the concurrence \mathcal{C} , which for a non-separable bipartite system $\mathcal{C} > 0$ and reaches unity for a maximally entangled state. Here we estimate a lower bound for the concurrence using the raw and background-corrected coincidences recorded in the experiment (shown in Figures 3b-c of the main text). The concurrence is given by

$$\mathcal{C} = \max(0, \sqrt{\lambda_0} - \sum_{i=1}^N \sqrt{\lambda_i}), \quad (60)$$

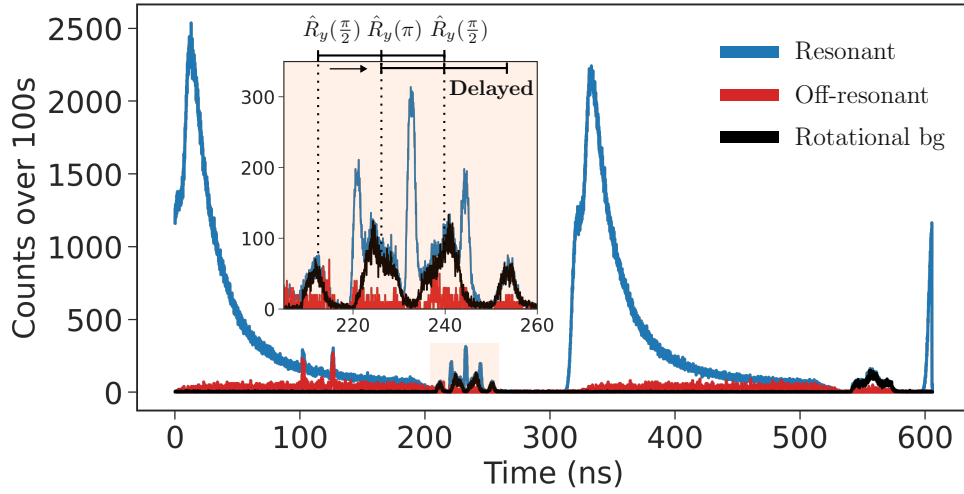
where λ_i are eigenvalues of the matrix $\rho_{\text{meas}}(\hat{\sigma}_y^{(p)} \otimes \hat{\sigma}_y^{(s)})\rho_{\text{meas}}(\hat{\sigma}_y^{(p)} \otimes \hat{\sigma}_y^{(s)})^\dagger$, and ρ_{meas} is the measured normalized density matrix of the spin-photon state assuming negligible off-diagonal entries [23]

$$\rho_{\text{meas}} = \begin{bmatrix} \rho_{e\uparrow, e\uparrow} & 0 & 0 & 0 \\ 0 & \rho_{e\downarrow, e\downarrow} & \rho_{l\uparrow, e\downarrow} & 0 \\ 0 & \rho_{e\downarrow, l\uparrow} & \rho_{l\uparrow, l\uparrow} & 0 \\ 0 & 0 & 0 & \rho_{l\downarrow, l\downarrow} \end{bmatrix}, \quad (61)$$

which shares the same form as Eq. (33). Using the coincidence counts in Figures 3b-c of the main text and Eq. (60), we find a raw (background-corrected) concurrence of $\mathcal{C} \geq 0.345 \pm 0.012$ (0.495 ± 0.105) with error bounds obtained by Monte Carlo simulations.

SUPPLEMENTARY NOTE 9: FIDELITY BACKGROUND SUBTRACTION

Background photons in this work include leakage from the photonic qubit and readout lasers, detector dark counts, accidental coincidence counts, and fluorescence from the rotational laser. Prior to running the experiment, both the optical paths for the photonic qubit and spin readout are optimized such that the signal-to-noise ratio is > 100 . The photon detection uses superconducting nanowire single-photon detectors (SNSPDs) with a dark count rate of 10 Hz.



Supplementary Figure 7. Entanglement pulse sequence overlaid with rotational background fluorescence. Fluorescence from the 350 GHz off-detuned rotational pulses near 200 ns can be seen in the time-resolved histogram recorded by the detectors. The inset shows a magnified view of the pulse sequence, where the background fluorescence from the rotational laser partially overlaps in time with the photon detection.

False coincidence counts account for $< 3\%$ of all detected coincidences. A majority of the background subtraction is done by removing the fluorescence during the rotational pulses which overlaps in time with the photon detection window, see inset of Supplementary Figure 7. The fluorescence may be due to photo-ionization by the red-detuned Raman laser [27] followed by subsequent reinjection of a hole, which leads to photon emission through the unfiltered cycling transition. This hypothesis could be supported by the fact that a 40 ns buffer pulse at 540 ns is used partly to inject a hole in the current device. The fluorescence from these pulses thus enters the detection path of the TBI and half of which is then delayed in time, partially overlapping with the time-bin detection windows.

-
- [1] Zhou, X. *et al.* High-efficiency shallow-etched grating on gas membranes for quantum photonic applications. *Applied Physics Letters* **113**, 251103 (2018).
 - [2] Chan, M. L. *et al.* Quantum state transfer between a frequency-encoded photonic qubit and a quantum-dot spin in a nanophotonic waveguide. *Phys. Rev. A* **105**, 062445 (2022).
 - [3] Witthaut, D. & Sørensen, A. S. Photon scattering by a three-level emitter in a one-dimensional waveguide. *New Journal of Physics* **12**, 043052 (2010).
 - [4] Das, S., Elfving, V. E., Reiter, F. & Sørensen, A. S. Photon scattering from a system of multilevel quantum emitters. ii. application to emitters coupled to a one-dimensional waveguide. *Phys. Rev. A* **97**, 043838 (2018).
 - [5] Kuhlmann, A. V. *et al.* Charge noise and spin noise in a semiconductor quantum device. *Nature Physics* **9**, 570–575 (2013).
 - [6] Appel, M. H. *et al.* Coherent spin-photon interface with waveguide induced cycling transitions. *Phys. Rev. Lett.* **126**, 013602 (2021).
 - [7] Besombes, L., Kheng, K., Marsal, L. & Mariette, H. Acoustic phonon broadening mechanism in single quantum dot emission. *Phys. Rev. B* **63**, 155307 (2001).
 - [8] Krummheuer, B., Axt, V. M. & Kuhn, T. Theory of pure dephasing and the resulting absorption line shape in semiconductor quantum dots. *Phys. Rev. B* **65**, 195313 (2002).
 - [9] Muljarov, E. A. & Zimmermann, R. Dephasing in quantum dots: Quadratic coupling to acoustic phonons. *Phys. Rev. Lett.* **93**, 237401 (2004).
 - [10] Tighineanu, P., Dreeßen, C. L., Flindt, C., Lodahl, P. & Sørensen, A. S. Phonon decoherence of quantum dots in photonic structures: Broadening of the zero-phonon line and the role of dimensionality. *Phys. Rev. Lett.* **120**, 257401 (2018).
 - [11] Urbaszek, B. *et al.* Nuclear spin physics in quantum dots: An optical investigation. *Rev. Mod. Phys.* **85**, 79–133 (2013).
 - [12] Merkulov, I. A., Efros, A. L. & Rosen, M. Electron spin relaxation by nuclei in semiconductor quantum dots. *Phys. Rev. B* **65**, 205309 (2002).
 - [13] Appel, M. H. *et al.* Entangling a hole spin with a time-bin photon: A waveguide approach for quantum dot sources of multiphoton entanglement. *Phys. Rev. Lett.* **128**, 233602 (2022).
 - [14] Gühne, O., Lu, C.-Y., Gao, W.-B. & Pan, J.-W. Toolbox for entanglement detection and fidelity estimation. *Phys. Rev. A* **76**, 030305 (2007).

- [15] Bodey, J. H. *et al.* Optical spin locking of a solid-state qubit. *npj Quantum Information* **5**, 95 (2019).
- [16] Appel, M. H. *A Quantum Dot Source of Time-Bin Multi-Photon Entanglement*. Ph.D. thesis, University of Copenhagen (2021).
- [17] Elfving, V. E., Das, S. & Sørensen, A. S. Enhancing quantum transduction via long-range waveguide-mediated interactions between quantum emitters. *Phys. Rev. A* **100**, 053843 (2019).
- [18] Shen, J.-T. & Fan, S. Strongly correlated multiparticle transport in one dimension through a quantum impurity. *Phys. Rev. A* **76**, 062709 (2007).
- [19] Le Jeannic, H. *et al.* Experimental reconstruction of the few-photon nonlinear scattering matrix from a single quantum dot in a nanophotonic waveguide. *Phys. Rev. Lett.* **126**, 023603 (2021).
- [20] Thyrrstrup, H. *et al.* Quantum optics with near-lifetime-limited quantum-dot transitions in a nanophotonic waveguide. *Nano Letters* **18**, 1801–1806 (2018).
- [21] Javadi, A. *et al.* Spin–photon interface and spin-controlled photon switching in a nanobeam waveguide. *Nature Nanotechnology* **13**, 398–403 (2018).
- [22] Dreiser, J. *et al.* Optical investigations of quantum dot spin dynamics as a function of external electric and magnetic fields. *Phys. Rev. B* **77**, 075317 (2008).
- [23] Nguyen, C. T. *et al.* An integrated nanophotonic quantum register based on silicon-vacancy spins in diamond. *Phys. Rev. B* **100**, 165428 (2019).
- [24] Bhaskar, M. K. *et al.* Experimental demonstration of memory-enhanced quantum communication. *Nature* **580**, 60–64 (2020).
- [25] Kalb, N., Reiserer, A., Ritter, S. & Rempe, G. Heralded storage of a photonic quantum bit in a single atom. *Phys. Rev. Lett.* **114**, 220501 (2015).
- [26] Antoniadis, N. O. *et al.* Cavity-enhanced single-shot readout of a quantum dot spin within 3 nanoseconds. *arXiv* **2210.13870** (2022).
- [27] Lochner, P. *et al.* Internal photoeffect from a single quantum emitter. *Phys. Rev. B* **103**, 075426 (2021).